The Astrophysical Journal, 856:94 (16pp), 2018 April 1 https://doi.org/10.3847/1538-4357/aab362
© 2018. The American Astronomical Society. All rights reserved.

Influence of the Solar Cycle on Turbulence Properties and Cosmic-Ray Diffusion

L.-L. Zhao[1,2], L. Adhikari[2], G. P. Zank[2,3,5], Q. Hu[2,3], and X. S. Feng[4]
[1] Key Laboratory of Computational Geodynamics, University of Chinese Academy of Sciences, Beijing, 100049, People's Republic of China
[2] Center for Space Plasma and Aeronomic Research (CSPAR), University of Alabama in Huntsville, Huntsville, AL 35805, USA
[3] Department of Space Science, University of Alabama in Huntsville, Huntsville, AL 35899, USA
[4] State Key Laboratory of Space Weather, National Space Science Center, Chinese Academy of Sciences, Beijing, 100190, People's Republic of China
Received 2018 January 13; revised 2018 February 26; accepted 2018 February 27; published 2018 March 28

Abstract

The solar cycle dependence of various turbulence quantities and cosmic-ray (CR) diffusion coefficients is investigated by using *OMNI* 1 minute resolution data over 22 years. We employ Elsässer variables $z^{\pm}$ to calculate the magnetic field turbulence energy and correlation lengths for both the inwardly and outwardly directed interplanetary magnetic field (IMF). We present the temporal evolution of both large-scale solar wind (SW) plasma variables and small-scale magnetic fluctuations. Based on these observed quantities, we study the influence of solar activity on CR parallel and perpendicular diffusion using quasi-linear theory and nonlinear guiding center theory, respectively. We also evaluate the radial evolution of the CR diffusion coefficients by using the boundary conditions for different solar activity levels. We find that in the ecliptic plane at 1 au (1), the large-scale SW temperature T, velocity V_{sw}, Alfvén speed V_A, and IMF magnitude B_0 are positively related to solar activity; (2) the fluctuating magnetic energy density $\langle z^{\pm 2}\rangle$, residual energy E_D, and corresponding correlation functions all have an obvious solar cycle dependence. The residual energy E_D is always negative, which indicates that the energy in magnetic fluctuations is larger than the energy in kinetic fluctuations, especially at solar maximum; (3) the correlation length λ for magnetic fluctuations does not show significant solar cycle variation; (4) the temporally varying shear source of turbulence, which is most important in the inner heliosphere, depends on the solar cycle; (5) small-scale fluctuations may not depend on the direction of the background magnetic field; and (6) high levels of SW fluctuations will increase CR perpendicular diffusion and decrease CR parallel diffusion, but this trend can be masked if the background IMF changes in concert with turbulence in response to solar activity. These results provide quantitative inputs for both turbulence transport models and CR diffusion models, and also provide valuable insight into the long-term modulation of CRs in the heliosphere.

Key words: cosmic rays – solar wind – Sun: activity – turbulence

1. Introduction

The transport of cosmic rays (CRs) throughout the heliosphere is determined by the large-scale solar wind (SW) flow and the turbulent fluctuations embedded in it. The background solar interplanetary magnetic field (IMF) periodically changes from solar maximum to minimum (~11 years), leading to variations in the different transport processes responsible for CR propagation, such as diffusion through the irregular IMF, outward convection by the SW, adiabatic deceleration, and gradient and curvature drifts (Potgieter 1998, 2013; Zhang 1999; Jokipii & Kóta 2000). As such, we can subsequently observe that CR intensities correlate inversely with solar activity due to solar-cycle-related changes in the modulation environment (Zhao & Zhang 2015, 2016). Numerical modeling describing time-dependent CR modulation in the heliosphere has progressed significantly over the past several decades (e.g., Le Roux & Potgieter 1995; Giacalone & Jokipii 1999; Ferreira & Potgieter 2004). For instance, 2D or 3D models based on solving the Parker transport equation (Parker 1965) are remarkably successful in simulating the observed temporal and spatial variations in the spectra from various spacecraft, ground-based neutron monitors, and balloon experiments (Manuel et al. 2011; Strauss et al. 2012; Zhao & Qin 2013; Zhao et al. 2014; Potgieter et al. 2015; Adriani et al. 2016). However, in the absence of a clear theory of how diffusion coefficients change with solar activity, most CR modulation models use empirical and phenomenological time-dependent diffusion coefficients based on observations of the magnetic field magnitude and variance. To understand the physical origin of the variation of the CR diffusion coefficients with solar activity, one needs to know how the diffusion coefficients depend on basic turbulence quantities (Bieber et al. 1995; Zank et al. 1998; Shalchi et al. 2004; Minnie et al. 2007; Burger et al. 2008; Shalchi 2009), such as the magnetic field turbulence energy and the correlation length scale, which may change with solar activity.

Energetic charged CR particles are scattered by small-scale magnetic field fluctuations in the IMF (Jokipii 1966). Thus, both turbulence and the large-scale SW flow control CR propagation within the heliosphere, implying a solar cycle dependence. Currently, there are several numerical models that couple CR transport with magnetic turbulence models and the evolving large-scale background throughout the heliosphere (e.g., Florinski et al. 2003; Engelbrecht & Burger 2013a, 2013b; Guo & Florinski 2016). Spacecraft observations show that local properties of the large-scale SW flow at 1 au are modulated by the solar cycle. There is evidence that greater mixing of fast and slow SW plasma typically occurs at solar maximum (e.g., Bame et al. 1976), and is more likely to depend on the latitude during solar minimum (Burger et al. 2000). It is, of course, also well established that the background IMF changes with solar cycle. However, a detailed understanding of the dependence of the turbulence quantities on solar activity, which is an important component of modeling

[5] Corresponding author.

the time-dependent modulation of CR particles in the heliosphere, is not yet well understood.

The evolution of low-frequency turbulent fluctuations in the large-scale radially expanding SW plasma can be interpreted in terms of magnetohydrodynamic (MHD) theory (Zhou & Matthaeus 1990a, 1990b). The WKB Alfvén wave model is the accepted paradigm for magnetized fluctuations in the SW flow, and describes the radial evolution of linear Alfvén waves in a slowly varying background (Matthaeus et al. 1994; Zank et al. 1996). It has been used to study the heliocentric and rigidity dependence of the CR diffusion tensor in the inner heliosphere (Völk et al. 1974; Morfill & Völk 1979; Chhiber et al. 2017). The WKB theory has several problems that make it inconsistent with a variety of different spacecraft observations (Zank et al. 2012). Two of the more notable deficiencies of the WKB theory are that (1) it cannot explain the changing Alfvén ratio r_A with heliocentric distance. In the inner heliosphere, the Alfvén ratio (the ratio of the kinetic to magnetic energy in fluctuations) $r_A \simeq 1$ (i.e., equipartition between kinetic and magnetic energy fluctuations). However, observations (Zank et al. 2012, 2017; Adhikari et al. 2015, 2017a, and references therein) indicate that the Alfvén ratio initially decreases slightly with heliocentric radial distance until about 4 au, after which it begins to increase significantly because of the presence of pickup-ion-driven turbulence in the outer heliosphere. Thus, the Alfvén ratio is not always approximately equal to 1 throughout the heliosphere. (2) Because it describes the propagation of linearized Alfvénic fluctuations, WKB theory cannot explain the observed non-adiabatic expansion of SW plasma in both the inner and outer heliospheres. Within 1 au, the heliocentric plasma temperature profile decays according to $\sim r^{-1.1}$ (Verma et al. 1995; Marino et al. 2008), which is slower than the adiabatic prediction $T(r) \propto r^{-4/3}$. *Voyager* and *Pioneer* observations (Gazis et al. 1995; Richardson & Smith 2003) show that, indeed, the temperature continues to decay at a rate slower than adiabatic, and even begins to increase slowly after ~20–30 au. The non-adiabatic evolution of the SW temperature with heliocentric distance requires an extended in situ heating source. This source has been ascribed to the decay of SW turbulence, both pre-existing and that generated in situ by processes such as stream–stream interactions, interplanetary shock waves, streaming energetic particles, and the creation of pickup ions in the distant heliosphere. In situ heating by turbulent dissipation can supply the energy to slow the temperature decay (Williams et al. 1995; Matthaeus et al. 1999; Smith et al. 2001, 2006; Isenberg 2005; Marino et al. 2008; Zank et al. 2012, 2017). Despite these and other limitations, WKB theory is remarkably accurate in describing the evolution of the magnetic energy density in SW fluctuations ($\propto r^{-3}$) within several astronomical units, consistent with the observed heliocentric evolution of magnetic power. The reconciliation of the successful but apparently mutually distinct WKB and turbulence descriptions was provided initially in Zank et al. (1996), who developed a turbulence transport model, restricted to a highly super-Alfvénic large-scale flow (i.e., $U \gg V_A$, with U the large-scale flow speed and V_A the Alfvén speed) and zero cross-helicity, to describe the radial decay of the magnetic fluctuation variance $\langle \delta B^2 \rangle$ from 1 to 40 au, and found close agreement between *Voyager 1* and *2* and *Pioneer* 11 data. In addition, the Zank et al. (1996) turbulence transport model reduces to the WKB model in the limit of no dissipation, driving, or nonlinear terms, or alternatively, if the rate of dissipation of turbulent fluctuations is balanced by the rate at which turbulent fluctuations are generated locally. Extensions of the Zank et al. (1996) model (e.g., Oughton et al. 2006, 2011; Zank et al. 2012, 2017; Wiengarten et al. 2016; Adhikari et al. 2017a) show that despite the decrease in fluctuating magnetic energy in the distant heliosphere, the increasing contribution by pickup-ion driving, especially beyond ~4 au, leads to an increase in the slab turbulence energy. With regard to the second problem, Williams et al. (1995) first estimated the heating of the SW due to the dissipation of turbulence, including that driven by pickup ions. Subsequently, Matthaeus et al. (1999) and Smith et al. (2001) extended the results of Zank et al. (1996) to nearly 80 au for the fluctuating magnetic energy and correlation length, and solved the SW temperature equation in which the dissipation of turbulence is included, successfully reproducing the observed SW temperature from 1 to 80 au. The evolution of the SW temperature due to the turbulent decay of fluctuations has since been invoked successfully in several turbulence models to reproduce the observed non-adiabatic SW temperature (e.g., Breech et al. 2008; Isenberg et al. 2010; Usmanov et al. 2011, 2014; Kryukov et al. 2012; Zank et al. 2012, 2017). Recently, Zank et al. (2017) have derived a coupled 2D and slab turbulence model that describes both components based on the theory of nearly incompressible (NI) MHD both in the context of homogeneous (Zank & Matthaeus 1992, 1993) and inhomogeneous (Hunana et al. 2008; Hunana & Zank 2010) flows. The model includes all basic turbulence variables, such as the fluctuation energy in forward and backward propagating modes, residual energy, cross-helicity, and correlation lengths, and shows extensive agreement with *Voyager 2* observations (Adhikari et al. 2017a). In addition, such a turbulence model with a dominant 2D component was also supported by the recent observational analysis of Zheng & Hu (2018), which confirmed the self-generation of inertial range structures in SW turbulence.

Once the turbulence model is determined, the CR diffusion coefficients can be derived from an appropriate energetic particle diffusion theory (Zank et al. 1998; Pei et al. 2010; Engelbrecht & Burger 2013a, 2013b, 2015; Chhiber et al. 2017; Engelbrecht 2017). Zhao et al. (2017) present a detailed analysis of the radial and rigidity dependence of the CR diffusion tensor using the Zank et al. (2017) two-component turbulence model, but consider only steady-state solutions with an assumed constant SW speed. Adhikari et al. (2014) studied solar cycle effects on the evolution of various turbulence quantities based on the Zank et al. (1996, 2012) model. The SW velocity, source terms, and inner boundary conditions are treated as time dependent. They find that the temporal SW introduces a periodic variability in the magnetic energy fluctuations and correlation length beyond 1 au. Chhiber et al. (2017) examine the effect of solar activity on CR parallel and perpendicular diffusion by varying the turbulence energy amplitude only (normal, half, and double turbulence energy) at the inner boundary, and find that solar activity increases perpendicular diffusion and reduces parallel diffusion.

Prior studies describing the evolution of turbulence variables and the related CR diffusion coefficients in the heliosphere use steady-state solutions or time-dependent empirical formula. In this paper, we use *OMNI* 1 minute resolution data to study the effect of solar cycle on the evolution of forward and backward turbulence energies, residual energy, and the corresponding

correlation functions at 1 au, which are essential to determine the CR diffusion coefficients. It is thought that SW fluctuations are highly anisotropic with respect to the direction of the large-scale mean magnetic field. Two-dimensional and slab modes provide a useful parameterization of anisotropy in SW turbulence (Duffy & Blundell 2005). Anisotropy is a local property of turbulence and depends on many factors, such as fast or slow SW, and high or low heliographic latitude, and it may also be affected by solar cycle. Several simulations and phenomenological studies have addressed the anisotropy of IMF fluctuations (e.g., Matthaeus et al. 2005; Osman & Horbury 2007; Weygand et al. 2009; Ruiz et al. 2011; Adhikari et al. 2017b). Dasso et al. (2005) suggest that SW fluctuations in the fast and slow SW exhibit different anisotropy properties, based on a statistical analysis of proton densities and magnetic and bulk velocity fields. They found that fast streams ($V_{sw} > 500\,km\,s^{-1}$) were dominated by fluctuations with quasi-parallel wave vectors, whereas for slow wind ($V_{sw} < 400\,km\,s^{-1}$), quasi-perpendicular modes were more dominant. Smith (2003) examined 530 intervals of *Ulysses* data, and found that the distribution of energy between slab and 2D wave vectors is approximately equal at high latitude during solar minimum. Oughton et al. (2015) concluded that most of the fluctuation energy resides in the vector components transverse to the mean field for the inertial range, whereas the variance anisotropy tends to become more isotropic in the dissipation range. A summary of the observed anisotropy results are listed in Table 1 of Oughton et al. (2015). For slow and intermediate SWs in the ecliptic plane at 1 au as used in our study, perpendicular (2D) wave vectors are a more dominant component (50%–85%) in the inertial range (see also Oughton et al. 2015, their Table 1). The 2D and slab energy ratio 80:20 is usually used in theoretical works based on the assumption of a plasma beta ~ 1 or $\ll 1$ in the SW or solar corona (e.g., Zank & Matthaeus 1992, 1993; Bieber et al. 2004; Hunana & Zank 2010; Zank et al. 2018). Adhikari et al. (2017b) investigated anisotropy in magnetic field fluctuations by assuming 80:20, 70:30, 60:40, and 55:45 initial energy ratios between 2D and slab turbulence at 1 au. They found that the evolving anisotropy ratios in both the energy-containing and inertial range are ordered by the inner boundary ratios, and exhibit similar trends for each initial anisotropy ratio. Here, we employ 2D and slab energy ratios of 80:20 and 60:40, respectively, to study the effect of this ratio on CR mean free paths. For the correlation scale variability in the IMF fluctuations, Osman & Horbury (2007) obtained a mean value of 1.79 ± 0.36 (with 0.36 the uncertainty) for the ratio of slab to 2D correlation lengths using 4 s resolution spin-averaged magnetic field data in a slow SW interval from the four *Cluster* spacecraft. Weygand et al. (2009, 2011) used 11 spacecraft data sets and found that the ratio of the slab to 2D correlation scales is 2.55 ± 0.76 (with 0.76 the uncertainty) for the slow SW, 2.15 ± 0.18 (with 0.18 the uncertainty) for the intermediate SW, and 0.71 ± 0.29 (with 0.29 the uncertainty) in the fast stream. Following prior studies (Pei et al. 2010; Dosch et al. 2013; Chhiber et al. 2017; Zhao et al. 2017), we assume that the ratio of the slab to 2D correlation scale is 2.0 because we consider slow and intermediate SW in the ecliptic plane at 1 au. Based on time-dependent 2D and slab turbulence quantities, we evaluate the CR parallel diffusion and perpendicular diffusion at 1 au for the two recent consecutive solar cycles according to quasi-linear theory (QLT; Jokipii 1966) and nonlinear guiding center (NLGC; Matthaeus et al. 2003) theory, respectively. More sophisticated CR diffusion theories have since been developed (e.g., Shalchi 2005, 2009; Shalchi et al. 2010; Ruffolo et al. 2012), but QLT and NLGC provide simple, reasonably tractable expressions that have been employed in many energetic particle transport studies (e.g., Zank et al. 1998, 2004; Pei et al. 2010; Effenberger et al. 2012; Zhao et al. 2017). For our purpose, they are sufficiently accurate. We also show the radial dependence of the CR diffusion coefficients derived from the Zank et al. (2017) NI MHD turbulence model for different solar activity levels. The inner boundary conditions and shear-driving source term are derived from observational data, and we then solve a system of 12 coupled 2D and slab turbulence equations that describes the radial evolution of several turbulence quantities. A detailed comparison between the turbulence solutions from the Zank et al. (2017) model using initial conditions that depend on solar activity levels and *Voyager 2* observations is in preparation (L. Adhikari et al. 2018, in preparation).

The organization of this paper is as follows: Section 2 presents briefly the minimum variance analysis (MVA) technique (Sonnerup & Scheible 1998) that enables us to decide the direction of the large-scale background IMF at 1 au, and thus the direction of a transverse fluctuation can be fixed. Section 3 presents the time-dependent evolution of various turbulence quantities using *OMNI* 1 minute resolution data, which are the input parameters for the Zank et al. (2017) NI MHD turbulence model. Section 4 illustrates the effect of solar activity on the evolution of the CR diffusion coefficients. The last section provides a summary and our conclusions.

2. Data Analysis

Numerous CR modulation studies have focused on solar minimum conditions (e.g., Zhao et al. 2014; Potgieter & Vos 2016). Since the CR diffusion coefficients require a number of turbulence quantities such as the 2D and slab variances of magnetic field fluctuations and the corresponding correlation lengths as input, long-term CR modulation requires knowledge of turbulence quantities over at least one solar cycle. Furthermore, turbulence transport models describing the radial evolution of such quantities in turn need the observed turbulence parameters in the inner heliosphere as input boundary conditions (Burger et al. 2014). Here, we use *OMNI* 1 minute resolution data sets from 1995 through 2017, covering about two consecutive solar cycles to calculate such turbulence quantities at 1 au. The method to find these quantities is similar to that of Zank et al. (1996) and Adhikari et al. (2015, 2017a). The various quantities are calculated for the inwardly and outwardly directed magnetic field separately, because the orientation of the IMF determines whether a mode is forward or backward propagating (Adhikari et al. 2017a; Zank et al. 2017). First, these turbulence quantities are calculated corresponding to the outwardly directed magnetic field only. For this case, all X components of the magnetic field (GSE coordinate system) in each interval should be negative. Otherwise, we discard the interval and then move to the next interval. Two criteria are used in each interval: (i) the mean square fluctuations of the velocity and magnetic field should be smaller than the square of the corresponding mean fields, and (ii) the intervals should contain at least $N/2$ good data points (N is the total number of data points in one interval). The process of calculating various turbulence quantities is as

follows: 2 hr interval data ($N = 120$) containing the X, Y, and Z components of the magnetic field and the SW velocity, the proton density, and temperature are taken. The missing data within an interval are discarded, then we check whether criteria (i) and (ii) are satisfied. Criterion (i) is used for all three components of the magnetic field and SW velocity, since it excludes intervals with irregular magnetic and velocity fluctuations. If one component does not meet criterion (i), the interval is discarded. Second, by following the same process, intervals corresponding to the inwardly directed magnetic field ($B_X > 0$) are selected. Various features of the SW plasma are speed related. For example, Dasso et al. (2005) found that the anisotropy of MHD-scale SW fluctuations differs in fast and slow SW. Observations show that the slab model corresponds predominantly to fast streams, and the 2D model corresponds predominantly to slow streams. Weygand et al. (2011) examined the correlation scales as a function of angle relative to the mean magnetic field direction for SW of different speeds. They found a monotonic transition from large anisotropy in slow SW to almost isotropy in fast SW. Since magnetic correlation scales are important to solar and galactic CR scattering, additional binning of data intervals by SW speed should be employed in future studies in CR diffusion. In this manuscript, we do not consider SW speed bins because more than 92% of the SW velocity is lower than 450 km s^{-1} after classification by criteria (i) and (ii) (see Figures 2(c) and 3(c)).

The next step in the analysis is to calculate the Elsässer variables (Elsässer 1950) in each retained interval corresponding to the inwardly and outwardly directed IMF, respectively. Before doing so, we need to find the direction of the background IMF, which is neither along the radial nor the azimuthal direction in the ecliptic plane at 1 au. We employ the MVA technique to find the direction of the background IMF, and then project the magnetic field and SW velocity vectors onto the two directions that are perpendicular to the background IMF direction, since we consider transverse fluctuations. This assumption allows us to regard the turbulent quantities as a superposition of 2D and slab fluctuations.

2.1. Minimum Variance Analysis

The MVA technique, applied to the observed magnetic field vector data, is used to find the direction normal to a transition layer in a plasma (Sonnerup & Scheible 1998). Here, we employ the MVA method to determine the unit vector of the background IMF in each interval from the measured magnetic field vector data. The detailed theory and derivation of the technique can be found in the references. We briefly introduce the basic equations that will be used in our data analysis. The fundamental MVA equation can be written in matrix form as

$$\sum_{\tau=1}^{3} M^{B}_{\sigma\tau} n_{\tau} = \eta n_{\sigma}, \tag{1}$$

where the subscripts σ, $\tau = 1$, 2, 3 denote the three components along a Cartesian coordinate system X, Y, and Z (e.g., GSE) in which the magnetic field vector data are given. n_{σ} and n_{τ} represent the components of a unit vector, η are scalar values, and the elements of a symmetric, 3×3 "magnetic variance matrix" are defined as

$$M^{B}_{\sigma\tau} \equiv \langle B_{\sigma} B_{\tau} \rangle - \langle B_{\sigma} \rangle \langle B_{\tau} \rangle, \tag{2}$$

where the brackets represent the mean values from any number of magnetic field measurements during an interval. This constitutes an eigenvalue problem for $M^{B}_{\sigma\tau}$. Therefore, as described in Sonnerup & Scheible (1998), the allowed η values are the eigenvalues η_1, η_2, and η_3 (given in descending order here) of the matrix $M^{B}_{\sigma\tau}$. Since $M^{B}_{\sigma\tau}$ is symmetric, the eigenvalues are all real and represent the actual variances in those field components. The corresponding eigenvectors, $\boldsymbol{x}_1$, $\boldsymbol{x}_2$, and $\boldsymbol{x}_3$, are orthogonal, and respectively represent the directions of maximum, intermediate, and minimum variation of the field components along each vector. The eigenvector $\boldsymbol{x}_3$, which corresponds to the smallest eigenvalue η_3, is in the direction of minimum variance and is assumed to be the direction of the background IMF. We use one criterion for rejecting degenerate solutions: the ratio of the intermediate to minimum eigenvalues needs to be greater than 2, i.e., $\eta_2/\eta_3 > 2$. The variance ellipsoid, as shown in the left panel of Figure 1 (see also Sonnerup & Scheible 1998), defines the variance along an arbitrarily chosen direction in the GSE coordinate system (X, Y, Z). Here, for example, η_1, η_2, and η_3 represent the variance of the magnetic field components along the eigenvectors $\boldsymbol{x}_1$, $\boldsymbol{x}_2$, and $\boldsymbol{x}_3$ respectively. We have selected a 2 hr interval (the 14th and 15th hours on 5/7/2009) as an example, which contains 120 good magnetic field component data corresponding to the inwardly directed IMF mode ($B_X > 0$). The calculated eigenvalues η_i ($i = 1, 2, 3$) $(nT)^2$ of this interval are as follows: $\eta_1 = 1.7 \times 10^{-2}$, $\eta_2 = 6.5 \times 10^{-3}$, and $\eta_3 = 9.72 \times 10^{-5}$. The corresponding eigenvectors in the GSE coordinate system are $\boldsymbol{x}_1 = (-0.61, -0.52, 0.59)$, $\boldsymbol{x}_2 = (-0.60, -0.18, -0.78)$, and $\boldsymbol{x}_3 = (0.51, -0.83, -0.21)$. The mean magnetic field $\langle \boldsymbol{B} \rangle = (2.25, -3.50, -0.72)$ (red line with arrow in Figure 1). From Figure 1, the direction with minimum variance is estimated to be along $\boldsymbol{x}_3$, which is very close to the mean magnetic field direction, and serves as an estimator for the direction of the background magnetic field. The right panel of Figure 1 shows the probability distribution of the angle between the direction of minimum variance and the mean field for the two solar cycles considered here. The angle mostly lies within 10°, which indicates that the mean magnetic field direction has the minimum variance in each interval. In addition, Burlaga et al. (2002) have compared the yearly averages of the magnetic field strength with the time-dependent Parker's model (Parker 1958) along the *Voyager 1* trajectory, and found consistency between the observed mean magnetic field and Parker spiral field. The minimum variance direction employed here may not necessarily agree with the direction of the Parker IMF since our value was calculated over a relatively short interval. Burlaga et al. (2002) also point out that Parker's spiral magnetic field model makes many assumptions, such as the SW moving radially away from some inner surface at a constant speed and being azimuthally symmetric about the solar rotation axis. These assumptions may not be valid for the variable solar wind speed on short timescales. The minimum variance direction we employed can coincide with the local mean field, but may not agree with the global large-scale field direction. We note that Cho & Vishniac (2000) and Milano et al. (2001) found that anisotropy in SW turbulence is more

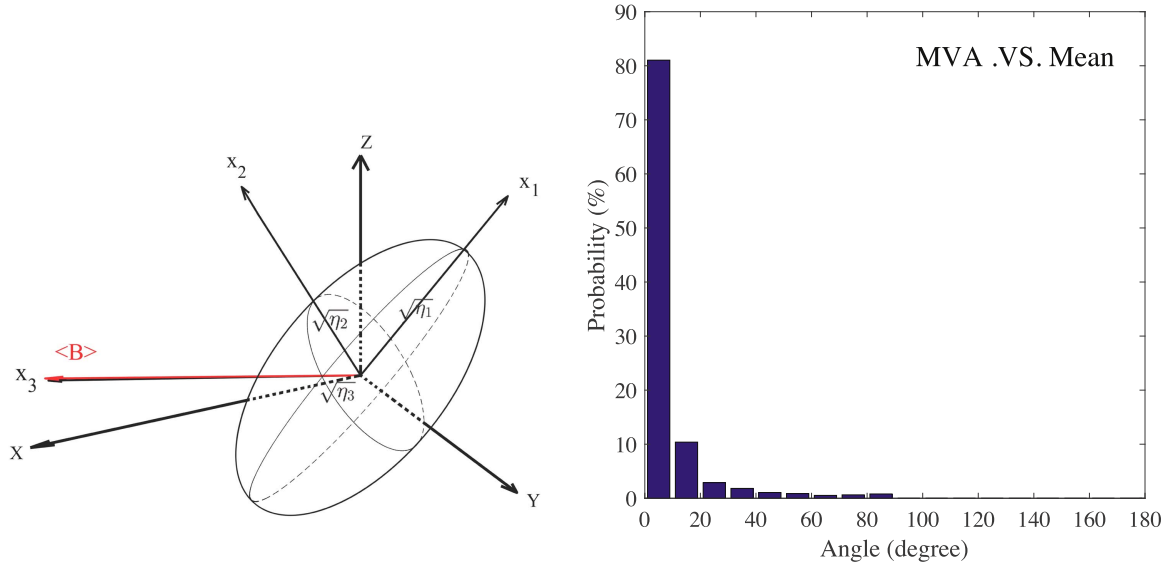

Figure 1. Left: the variance ellipsoid. η_1, η_2, and η_3 represent the variance of the magnetic field components along the eigenvectors $\boldsymbol{x}_1$, $\boldsymbol{x}_2$, and $\boldsymbol{x}_3$, respectively. Eigenvectors are shown relative to the GSE coordinate system (X, Y, Z) in which the magnetic field vector data are given. The direction of the background field is estimated to be along $\boldsymbol{x}_3$. The red line with an arrow represents the direction of the mean magnetic field $\langle \boldsymbol{B} \rangle$. Right: the probability of the angle between the direction with minimum variance and the mean field during 1995–2017.

pronounced when the mean magnetic field is computed over a smaller region. Chen et al. (2011) and Matthaeus et al. (2012) also confirmed that Alfvénic fluctuations in SW turbulence reflect the local mean field more than the global large-scale field, and suggested a larger anisotropy when the mean field is computed locally. Therefore, our assumption of the 2D and slab energy ratio (80:20 and 60:40, respectively) seems reasonable based on the use of two hourly averaged bins.

In the following calculations, we first compute the orthonormal basis ($\boldsymbol{x}_1$, $\boldsymbol{x}_2$, $\boldsymbol{x}_3$) using the MVA method in each interval, and $\boldsymbol{x}_3$ (denoted as X' in the following for brevity) represents the minimum variance direction, which coincides with the local mean field direction. Second, the observed magnetic field and velocity field components in each interval are mapped into $\boldsymbol{x}_1$ and $\boldsymbol{x}_2$ (denoted as Y' and Z') directions, since we consider transverse turbulent fluctuations. The MVA method can easily determine three directions in each interval: one represents the mean field direction, and the other two represent the direction perpendicular to the mean field.

2.2. Fluctuation Energy and Correlation Lengths

Fluctuating magnetic and velocity fields can be separated from their mean fields as $\underline{\boldsymbol{B}} = \boldsymbol{B} + \boldsymbol{b}$; $\underline{\boldsymbol{U}} = \boldsymbol{U} + \boldsymbol{u}$. Here, $\boldsymbol{B}$ is the mean magnetic field, $\boldsymbol{U}$ is the mean velocity field, and $\boldsymbol{b}$ and $\boldsymbol{u}$ are the fluctuating fields. Here, $\langle \underline{\boldsymbol{B}} \rangle = \boldsymbol{B}$ and $\langle \boldsymbol{b} \rangle = 0$, and so too with the velocity field. Zank et al. (2017) rewrote the NI MHD system to describe the transport of the majority of the 2D and minority slab turbulence in terms of Elsässer variables throughout the heliosphere, which provides a more refined framework to investigate turbulence in sub- and super-Alfvénic SW flow. Here, we investigate the solar-cycle-related input parameters for the Zank et al. (2017) two-component turbulence model from which we study the influence of solar activity on the CR diffusion tensor. We first introduce the definition of the Elsässer variables:

$$z^{\pm} = \boldsymbol{u} \pm \frac{\boldsymbol{b}}{\sqrt{\mu_0 \rho}}, \tag{3}$$

where μ_0 is the magnetic permeability and ρ is the mass density. The Elsässer variables $z^{\pm}$ are functions of both large-scale spatial coordinates and small-scale coordinates, in which z^{+} (z^{-}) represents the forward (backward) propagating modes with respect to the IMF orientation. The background plasma variables $\boldsymbol{U}$ (mean velocity field), $\boldsymbol{V}_A$ (Alfvén velocity), T (SW temperature), and N (SW density) depend on the large-scale coordinates. We further introduce the following moments of the Elsässer variables $z^{\pm}$ (Zank et al. 2012):

$$\langle z^{+2} \rangle \equiv \langle \boldsymbol{z}^{+} \cdot \boldsymbol{z}^{+} \rangle = \langle u^2 \rangle + \langle b^2 / \mu_0 \rho \rangle + 2 \langle \boldsymbol{u} \cdot \boldsymbol{b} / \sqrt{\mu_0 \rho} \rangle, \tag{4}$$

$$\langle z^{-2} \rangle \equiv \langle \boldsymbol{z}^{-} \cdot \boldsymbol{z}^{-} \rangle = \langle u^2 \rangle + \langle b^2 / \mu_0 \rho \rangle - 2 \langle \boldsymbol{u} \cdot \boldsymbol{b} / \sqrt{\mu_0 \rho} \rangle, \tag{5}$$

$$E_D \equiv \langle \boldsymbol{z}^{+} \cdot \boldsymbol{z}^{-} \rangle = \langle u^2 \rangle - \langle b^2 / \mu_0 \rho \rangle. \tag{6}$$

Here, $\langle z^{+2} \rangle$ and $\langle z^{-2} \rangle$ respectively represent the energy density in the forward and backward propagating modes. E_D is the energy difference in the fluctuation energy (also called the residual energy). According to CR diffusion theory, we need to calculate the 2D and slab turbulence magnetic energies as input for the CR diffusion coefficients. Here, we first calculate the total fluctuating magnetic energy $\langle b^2 \rangle$ using

$$\langle b^2 \rangle = \frac{\langle z^{+2} \rangle + \langle z^{-2} \rangle - 2E_D}{4} \mu_0 \rho. \tag{7}$$

Then, we assume that the total energy in fluctuations can be divided into majority 2D and minority slab energies with two sets of fixed ratios, 80:20 (Zank & Matthaeus 1992, 1993; Bieber et al. 1996) and 60:40 (Oughton et al. 2015; Adhikari et al. 2017b),

respectively. To calculate the correlation lengths of the 2D and slab fluctuations, 2 hr interval data sets are considered, provided each interval contains 120 good data points ($N = 120$). First, the Y' and Z' components of the Elsässer variables z^+ and z^- are calculated in each interval. Then, for the Elsässer variables $z^{\pm}$ and the lagged variables $z^{\pm\prime}$, the correlation functions can be defined using a spatial lag r with $r = V_{sw}t$, where V_{sw} is the averaged SW speed in each interval and t is the time lag, and are given by

$$L^+ \equiv \int \langle z^+ \cdot z^{+\prime} \rangle dr \equiv \langle z^+ \cdot z^+ \rangle \lambda^+ = \lambda^+ \langle z^{+2} \rangle, \quad (8)$$

$$L^- \equiv \int \langle z^- \cdot z^{-\prime} \rangle dr \equiv \langle z^- \cdot z^- \rangle \lambda^- = \lambda^- \langle z^{-2} \rangle, \quad (9)$$

$$L_D \equiv \int \langle z^+ \cdot z^{-\prime} + z^{+\prime} \cdot z^- \rangle dr \equiv \lambda_D E_D. \quad (10)$$

Here, $L^{\pm}$ and $\lambda^{\pm}$ are the correlation functions and correlation lengths corresponding to the energy density of the forward/backward propagating model $\langle z^{\pm 2} \rangle$, respectively. L_D and λ_D are the correlation function and correlation length corresponding to the residual energy E_D, respectively. Note that we directly calculate the three correlation functions L^+, L^-, and L_D instead of the correlation lengths λ^+, λ^-, and λ_D for the Elsässer variables. After calculating the correlation functions through the above integral form, we can obtain the fluctuating magnetic field variance correlation length λ as follows (Equation (76) in Zank et al. 2017):

$$\lambda = \frac{L^+ + L^- - L_D}{\langle z^{+2} \rangle + \langle z^{-2} \rangle - 2E_D}. \quad (11)$$

As with previous studies, the slab correlation length λ_s is assumed to be twice the 2D correlation scale λ_{2D}, thus $\lambda_s = 2\lambda_{2D} = 2\lambda$ (Pei et al. 2010; Dosch et al. 2013; Chhiber et al. 2017).

3. Results

In this section, we present observations of both the large-scale background plasma variables and small-scale fluctuation quantities at 1 au from 1995 to 2017, which will be used as input boundary conditions for the Zank et al. (2017) turbulence model. In L. Adhikari et al. (2018, in preparation), we show the radial evolution of these quantities using different solar-activity-related boundary conditions, and compare the numerical results with observations from *Voyager 2*. Here, we evaluate the CR parallel and perpendicular diffusion coefficients based on the above 2D and slab turbulence magnetic energy and correlation lengths at 1 au for two solar cycles according to QLT and NLGC theory, respectively. Finally, we present the radial evolution of the parallel and perpendicular diffusion coefficients for different solar activity levels using the turbulence solutions from L. Adhikari et al. (2018, in preparation).

3.1. Input Parameters for Turbulence Models

Figures 2 and 3 show the temporal evolution of the SW temperature T, density N, velocity V_{sw}, Alfvén velocity V_A, and heliospheric magnetic field magnitude B at 1 au as recorded by *OMNI* during 1995–2017. Mean values of each parameter in each interval are calculated for the inwardly and outwardly directed IMF, respectively. Red circles represent yearly averaged values of these large-scale parameters, and the solid circles represent three epochs (year 2003, 2009, and 2015) with different solar activity levels. We present the radial evolution of CR diffusion coefficients for these three years below. As a reference, we present the monthly averaged sunspot number (SSN) to evaluate the level of solar activity. The SW temperature T, velocity V_{sw}, Alfvén speed V_A, and heliospheric magnetic field magnitude B exhibit a similar variable trend to the solar cycle distribution of the SSN. However, the SW density N shows little correlation with solar activity. There is some anti-correlation between temperature and density, but it is not clear in solar cycle 24. Remarkably, T, V_{sw}, V_A, and B all reached a maximum value in 2003 during solar cycle 23 and a weak peak in 2015 during solar cycle 24, and have a lag of $\sim$1 year with respect to the corresponding peak of the SSN. Note that we do not focus on the specific peak time in this study since there are some other estimators of solar activity, e.g., coronal mass ejection, which is a striking manifestation of solar activity seen in the solar corona and also has a delay timescale of $\sim$11 months with respect to the SSN (Wheatland & Litvinenko 2001; Du 2012).

Figures 4 and 5 show the temporal evolution of the energy density in the forward and backward propagating modes $\langle z^{\pm 2} \rangle$ and the corresponding correlation functions $L^{\pm}$, the residual energy E_D, and the corresponding correlation function L_D. Figure 4 shows the data sets for two solar cycles for the inwardly directed IMF, and Figure 5 is for the outwardly directed IMF. All of the small-scale turbulence quantities of Figures 4 and 5 are derived from Equations (4)–(6) and (8)–(10). The red circles represent yearly averaged values for these quantities, and years 2003, 2009, 2015 are also selected as representative of the three special periods (red solid circles). From Figures 4 and 5, we can see that all turbulence quantities vary with solar activity and show solar cycle dependence. It is interesting to see that the values of the residual energy E_D and the corresponding correlation function L_D are always negative, which illustrates that the energy in magnetic fluctuations is larger than the energy in kinetic fluctuations, especially at solar maximum. E_D and L_D are both anti-correlated with solar activity while the other two energy densities and associated correlation functions are positively correlated with solar cycle. $\langle z^{+2} \rangle$, $\langle z^{-2} \rangle$, E_D, L^+, L^-, and L_D are all calculated using two-hour intervals ($N = 120$). In addition, Shiota et al. (2017) have analyzed extensively the effect on correlation lengths when using longer intervals. They found that a longer interval data set may not be helpful in determining correlations within the inertial range of turbulence in the SW. This is because a longer interval may introduce some structures associated with large-scale flows into the analysis, which then leads to an increase in the correlation functions and correlation lengths. For our analysis, 2 hr is the most suitable length of interval that yields reasonable correlation lengths when compared with *Voyager 2* observations (L. Adhikari et al. 2018, in preparation). We assume that the maximum time lag t is 1 hr ($N/2$ data points) when calculating the correlation functions in Equation (8)–(10). Most previous studies use the spatial lag r, where the auto-correlation function of the Elsässer variable becomes $1/e$ of the maximum values, to determine the correlation length. Since the auto-correlation function of the Elsässer variable drops rapidly, a spatial lag at $1/e$ of the maximum value is closer to zero lag. Therefore, limiting our analysis to a maximum time lag seems reasonable. Besides, the temporal evolution of the energy

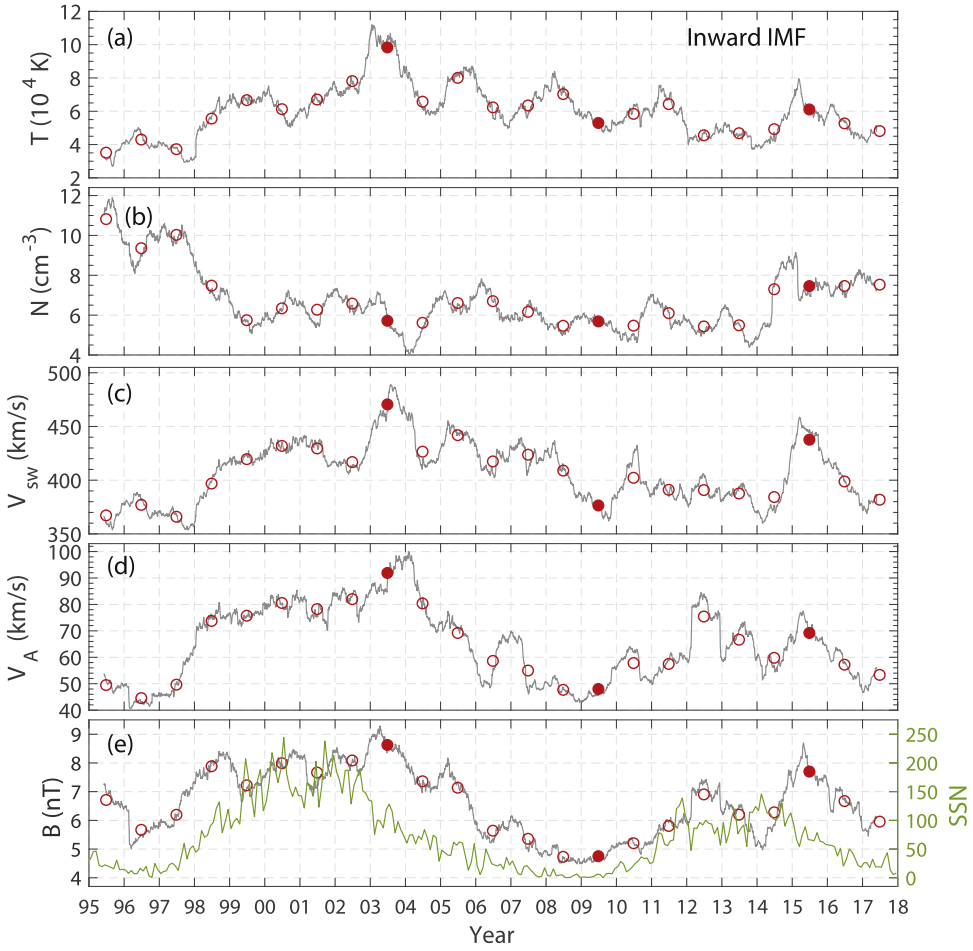

Figure 2. Temporal evolution of (a) proton temperature T, (b) density N, (c) solar wind velocity V_{sw}, (d) Alfv́en velocity V_A, and (e) heliospheric magnetic field magnitude B at 1 au for the inwardly directed IMF. Red circles represent the yearly averaged values of each parameter with three solid circles representing years 2003, 2009, and 2015, respectively. The green line in the bottom panel shows the monthly averaged sunspot number (SSN).

density (also the residual energy) and the corresponding correlation functions looks similar, which illustrates that the Elsässer variables $z^{\pm}$ and the lagged Elsässer variables $z^{\pm\prime}$ are quite well correlated when using the above maximum time lag.

Figure 6 depicts the influence of solar activity on a critical term in the shear source expression of the 2D and slab turbulence transport equations. The monthly mean SSN is also given as a reference. The complete form of the shear source terms that we consider is given by Zank et al. (2017) as

$$S_{\langle z^{\pm 2}\rangle} = C_{\rm sh}^{\pm}\frac{r_0|\Delta U|V_A^2}{r^2}; \qquad S_{E_D} = C_{\rm sh}^{E_D}\frac{r_0|\Delta U|V_A^2}{r^2}, \quad (12)$$

where the parameters $C_{\rm sh}^{\pm}$ and $C_{\rm sh}^{E_D}$ are the parameterized strengths of the shear source of energy in the forward and backward modes and the residual energy, respectively. $C_{\rm sh}^{+} \neq C_{\rm sh}^{-} \geqslant 0$, and $C_{\rm sh}^{E_D}$ can be 0, positive, or negative. r_0 is a reference location. ΔU is the difference between fast and slow SW speeds, and V_A is the background Alfv́en speed. In Figure 6, we calculate the product $\Delta U V_A^2$ in each 96 hr interval to include the structure of streams. The red circles are the yearly averaged values of $\Delta U V_A^2$, and the solid circles represent the years 2003, 2009, and 2015, respectively. The green line is calculated in the time interval determined by start and end times of each stream interaction region (SIR) event during 1995–2009, which were compiled by Jian et al. (2006, 2011). Our result agrees well with the SIR list for 1995–2009, and shows a rather clear solar cycle dependence, which indicates that the shear source term of turbulence is also correlated with solar activity.

Figures 2–6 show all the quantities that are needed in our turbulence model. All quantities exhibit either a correlation or anti-correlation with solar activity. For inwardly and outwardly directed IMF, all of the quantities have similar evolution properties, which indicate that small-scale fluctuations exhibit at best a weak dependence on the direction of the background magnetic field. For the shear source term, we do not need to distinguish the direction of the IMF. The values of all these quantities in the years 2003, 2009, and 2015 are shown in Tables 1 and 2 for the inwardly and outwardly directed IMF, respectively. These will be used as input parameters for the inner boundary condition in our turbulence model. In the following section, we use these solar-cycle-related turbulence quantities to investigate their effects on CR diffusion.

3.2. The Effects of Solar Activity on CR Diffusion

Figure 7 shows the monthly averaged 2D and slab turbulence magnetic energies and the corresponding correlation lengths calculated, respectively, from Equations (7) and (11). The red dashed lines are for inwardly directed IMF, and the blue lines for outwardly directed IMF. We can see that there is little

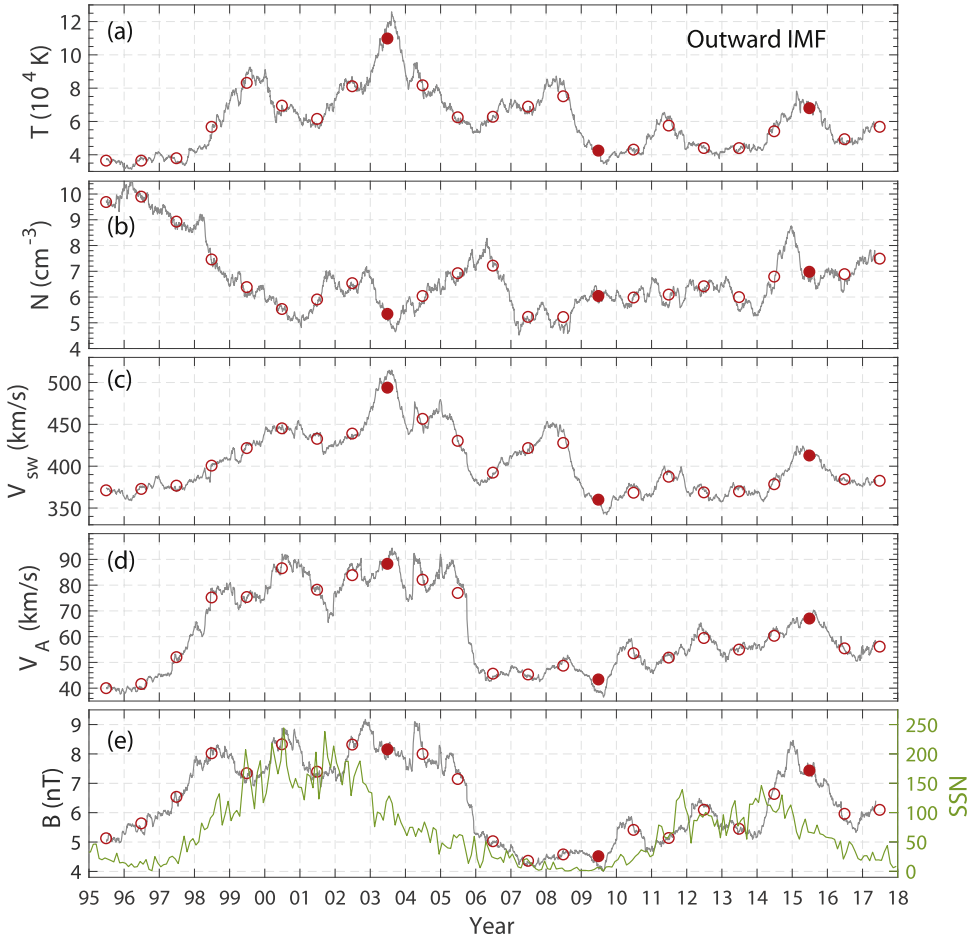

Figure 3. Same as Figure 2, but now for the outwardly directed IMF.

difference in the temporal evolution of these quantities between the inwardly and outwardly directed IMF modes. $\langle b_{2D}^2\rangle$: $\langle b_s^2\rangle = 80\%$: 20% and $\lambda_s = 2\lambda_{2D} = 2\lambda$ have been assumed in this figure. We can see a clear solar cycle dependence in the turbulence energy. Solar maximum carries more turbulent energy than solar minimum, which is caused by the frequent generation of shocks that generate turbulence (Zank et al. 1996; Adhikari et al. 2016). In contrast, the correlation lengths show no discernible solar cycle variation; in other words, the variation is very small. Wicks et al. (2009) studied the spatial correlation properties of the SW in the ecliptic at 1 au using *ACE* and *Wind* measurements, and found that the correlation length for components of the magnetic field does not show an obvious solar cycle dependence, which is consistent with our results. From Figure 7, we notice that the slab turbulence energy $\langle b_s^2\rangle$ in year 2003 is four times larger than that in year 2009, and the correlation length λ_s in 2003 is two times larger than in 2009. The averaged value of λ_s is about 0.88×10^6 km. This value is a little smaller than previous studies of correlation lengths for magnetic field fluctuations in the SW. For example, Tu & Marsch (1995) gave a value of the correlation length for the Elsässer variables as $\lambda \approx 265R_E \approx 1.7 \times 10^6$ km using single-spacecraft measurements. Matthaeus et al. (2005) investigated the value of λ using multiple-spacecraft measurements, and suggested a value of $\lambda \approx 1.3 \times 10^6$ km. Matthaeus et al. (2008) discussed the difference between multiple- and single-spacecraft measurements of the correlation length. However, these previous results did not consider the effect of solar activity levels on correlation lengths.

Figures 8 and 9 show the effects of solar activity on the CR parallel $\lambda_\parallel$ (blue line), perpendicular $\lambda_\perp$ (red line), and radial mean free path λ_{rr} (gray line) for a proton with rigidity 445 MV (corresponding to a 100 MeV proton) for the inwardly and outwardly directed IMF, respectively. As described in Zank et al. (1998), the parallel mean free path (mfp) based on standard QLT and assuming magnetostatic turbulence is approximated by

$$\lambda_\parallel = 6.2742\frac{B_0^{5/3}}{\langle b_s^2\rangle}\left(\frac{P}{c}\right)^{1/3}\lambda_s^{2/3}\left[1+\frac{7A/9}{(q+1/3)(q+7/3)}\right], \tag{13}$$

where $q = \frac{5s^2/3}{1+s^2-(1+s^2)^{1/6}}$, $A = (1+s^2)^{5/6} - 1$, and $s = 0.746834R_L/\lambda_s$. R_L is the particle Larmor radius, P is the particle rigidity, and B_0 is the mean magnetic field strength. The analytic form of the perpendicular mfp based on NLGC theory is given by (Zank et al. 2004; Shalchi et al. 2010)

$$\lambda_\perp = \left[\sqrt{3}\,\pi a^2 C\frac{\langle b_{2D}^2\rangle}{B_0^2}\lambda_{2D}\right]^{2/3}\lambda_\parallel^{1/3}, \tag{14}$$

where $a^2 = 1/3$ is a factor related to the gyrocenter velocity. $C = \Gamma(\nu)/[2\sqrt{\pi}\Gamma(\nu - 1/2)]$ is a constant such that $\nu = 5/6$ yields a Kolmogorov (1941) spectrum. Note that Equation (14)

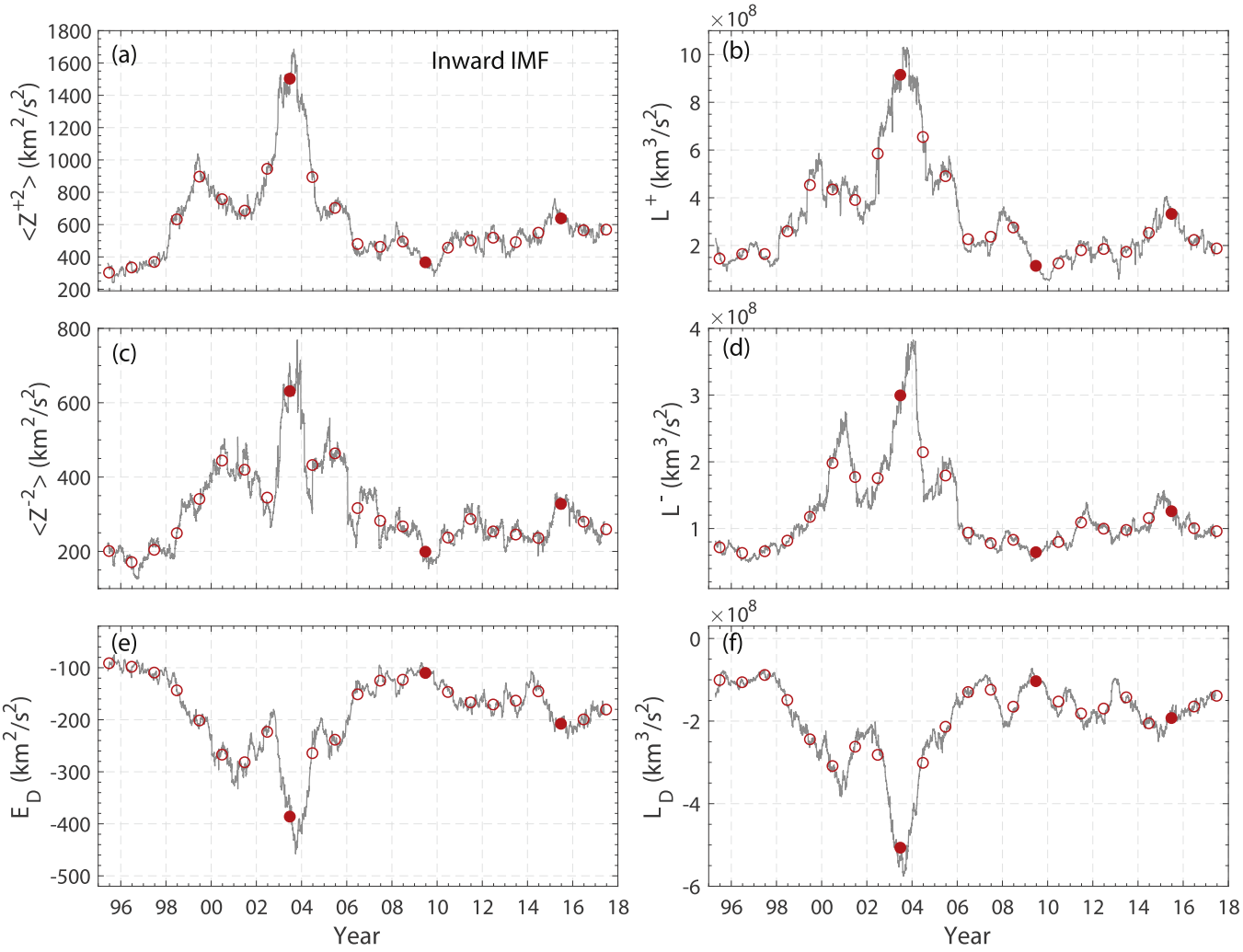

Figure 4. Temporal evolution of (a) the energy density in forward propagating modes $\langle z^{+2}\rangle$ and (b) the corresponding correlation function L^{+}; (c) the energy density in backward propagating modes $\langle z^{-2}\rangle$ and (d) the corresponding correlation function L^{-}; and (e) the residual energy E_D and (f) the corresponding correlation function L_D for the inwardly directed IMF. Red circles represent the yearly averaged values of each parameter. Red solid circles represent years 2003, 2009, and 2015, respectively.

was derived under the assumption of a specific form of 2D wave spectrum, which is a constant at large turbulence scales. It means that the 2D turbulence spectrum is independent of wavenumber in the energy range in Equation (14). Observation of magnetic fluctuations in the SW indicates that omnidirectional power spectra approach a k^{-1} wavenumber dependence and that low-frequency turbulence exhibits some sunspot cycle variability (Bieber et al. 1991). Based on this, Engelbrecht & Burger (2015) derived the perpendicular mfp by specifying the energy range spectral index of 2D turbulence power spectra as -1. A more general form of the 2D power spectrum with an energy range spectral index q was proposed by Shalchi et al. (2010). They show that the spectral index has a strong influence on the perpendicular diffusion coefficient. In their model, negative values of q correspond to a decreasing spectrum in the energy range, $q = 0$ corresponds to the constant spectrum we use here, and positive values of q correspond to an increasing spectrum. Matthaeus et al. (2007) presented a similar spectrum in different regimes: energy range, inertial range, and intermediate regime where the spectrum is proportional to k^{-1} to coincide with observations (Bieber et al. 1991; Goldstein & Roberts 1999). However, Shalchi (2013) argues that a spectrum that behaves like k^{-1} does not provide a different perpendicular diffusion coefficient (see also Shalchi et al. 2010), since the field lines for such length scales behave superdiffusively as in the inertial range (Shalchi & Kourakis 2007). In view of this uncertainty, we do not take into account a more elaborate spectrum in the present paper. The behavior of the 2D wave spectrum in the energy range, which may also be correlated with the sunspot cycle, is an important factor in deriving the CR perpendicular mfp. A general form (e.g., Shalchi et al. 2010; Shalchi 2013) should be employed in future studies of CR diffusion.

The radial mfp, λ_{rr}, can be expressed as a function of the heliospheric magnetic field winding angle ψ,

$$\lambda_{rr} = \lambda_{\parallel}\cos^2\psi + \lambda_{\perp}\sin^2\psi, \tag{15}$$

where $\tan\psi = B_Y/B_X$, and B_X (B_Y) is the average X (Y) component of the magnetic field in each interval. The winding angle therefore is not a constant in our calculation, but varies with time. In Figures 8 and 9, we employ the monthly averaged 2D and slab turbulence energy and corresponding correlation

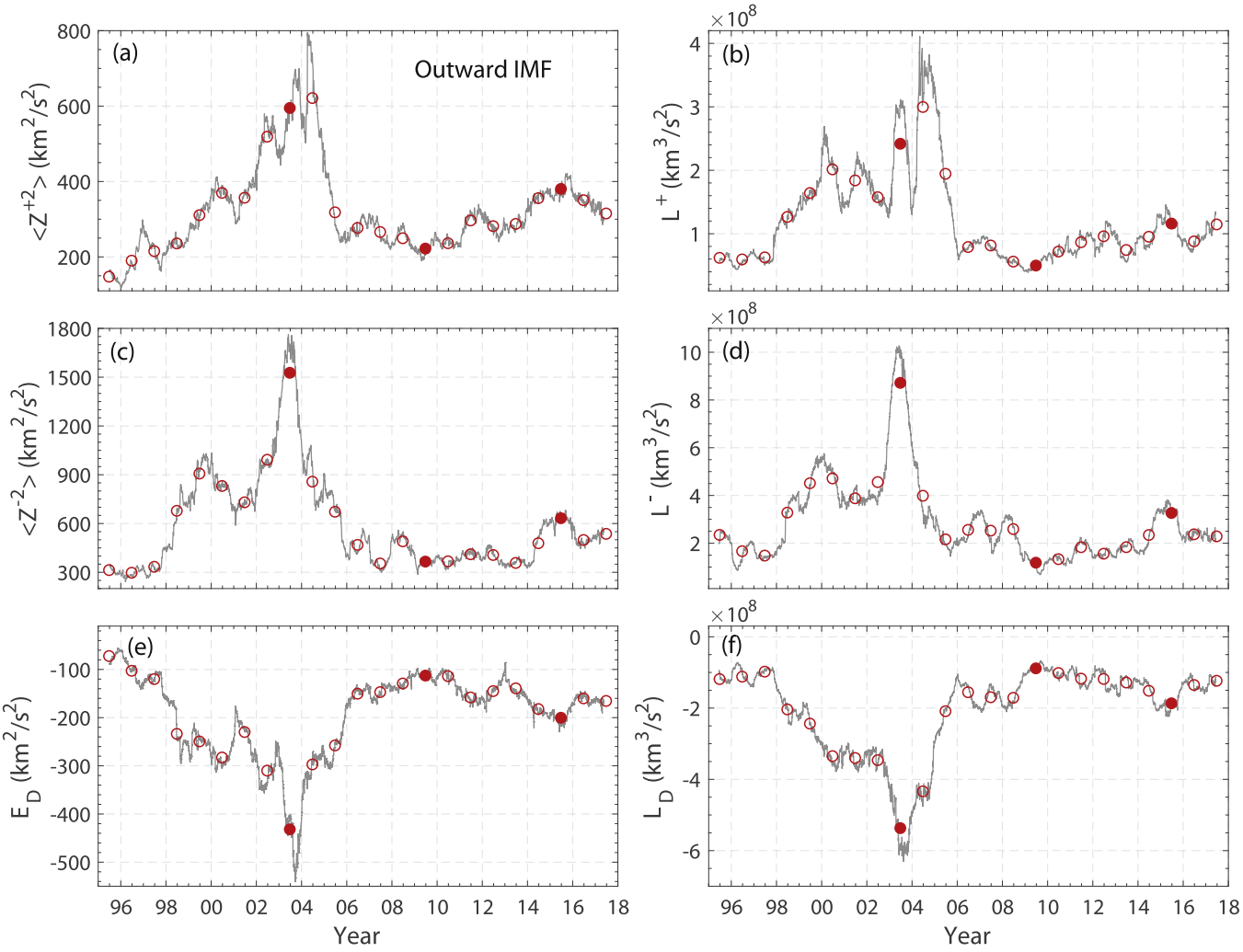

Figure 5. Same as Figure 4, but now for the outwardly directed IMF.

lengths shown in Figure 7 to calculate CR mfp's in the ecliptic plane at 1 au. In these two figures, we use a mean value of $B_0 = 5.5$ nT at 1 au to focus on the effects of the small-scale turbulence quantities on the CR diffusion coefficients. From Figures 8 and 9, we can clearly see the solar cycle dependence of $\lambda_\parallel$, $\lambda_\perp$, and λ_{rr}. The parallel mfp $\lambda_\parallel$ during solar maximum (i.e., 2003) is lower than that during solar minimum (i.e., 2009). In contrast, the perpendicular mfp $\lambda_\perp$ in the solar maximum is higher than that in the solar minimum. $\lambda_\parallel$ is nearly three orders of magnitude larger than the perpendicular mfp $\lambda_\perp$ at 1 au. The radial mfp λ_{rr} is dominated by parallel diffusion $\lambda_\parallel$ in the inner heliosphere (Zhao et al. 2017) and also has a positive correlation with solar activity. Chhiber et al. (2017) studied the influence of solar activity on the CR parallel and perpendicular diffusion in the inner heliosphere. They found that increasing the turbulence magnitude leads to a decrease in parallel mfp and an increase in perpendicular mfp, which is in agreement with Figures 8 and 9, where we assumed a fixed value of B_0.

In Figure 10, we use the solar-cycle-dependent background IMF magnitude obtained from Figure 3(e) to calculate the parallel $\lambda_\parallel$ (blue lines), perpendicular $\lambda_\perp$ (red lines), and radial λ_{rr} (cyan lines) mfp's for the outwardly directed IMF. Two-dimensional and slab fluctuation magnetic energies and the corresponding correlation lengths are the same as in Figures 8 and 9. By considering the variation of both turbulence quantities and the background IMF magnitude, we find that the solar cycle dependence of the CR mfp's is reduced, since the background IMF magnitude B_0 and turbulence energy $\langle b_s^2 \rangle$ (or $\langle b_{2D}^2 \rangle$) each have the opposite effect on $\lambda_\parallel$ (or $\lambda_\perp$), as shown by Equations (13) and (14). For example, for a fixed value of the background IMF, an increase in $\langle b_s^2 \rangle$ leads to a decrease in $\lambda_\parallel$ as shown in Figure 9, while for a fixed $\langle b_s^2 \rangle$, an increase in B_0 leads to an increase in $\lambda_\parallel$. Therefore, when we take into account both effects, the solar cycle dependence of $\lambda_\parallel$ is somewhat masked but still identifiable. It is interesting to see that there is an anti-correlation between the parallel mfp $\lambda_\parallel$ and the perpendicular mfp $\lambda_\perp$. For this $\langle b_{2D}^2 \rangle$: $\langle b_s^2 \rangle$ = 80: 20 case, the averaged value of $\lambda_\parallel$ is about 0.9 au, and the averaged value of $\lambda_\perp$ is about 1.6×10^{-3} au.

In Figure 11, we assume the ratio $\langle b_{2D}^2 \rangle$: $\langle b_s^2 \rangle$ = 60: 40 to examine the effect of turbulence anisotropy on CR mfp's. All other quantities are the same as in Figure 10, including the observed solar-cycle-dependent IMF magnitude B_0. For the 60:40 2D and slab energy ratio, there is little difference in the temporal tendency of each mfp. There is again a reduced solar cycle dependence of the CR mfp's when the variations of the turbulence quantities and IMF magnitude are both considered.

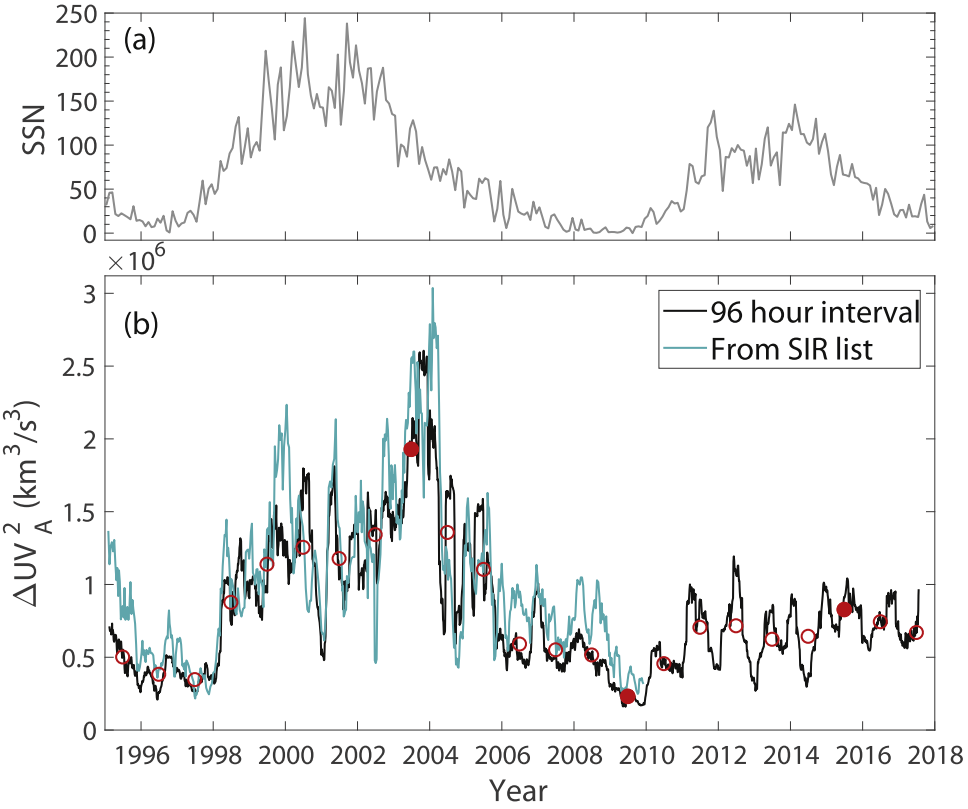

Figure 6. Top panel (a) shows the monthly averaged sunspot number (SSN). Panel (b) shows the temporal evolution of the shear source term ΔUV_A^2 at 1 au. The black line represents the result calculated in each 96 hr interval, and the red circles represent the yearly averaged values. The green line represents the result calculated in the time interval determined by start and end times of each shear interaction region (SIR) event during 1995–2009. The red solid circles represent years 2003, 2009, and 2015, respectively.

Table 1
Initial Conditions at 1 au for the Inwardly Directed IMF

	Year 2003	Year 2009	Year 2015
$\langle z^{+2}\rangle$	1500.31 km^2 s^{-2}	363.99 km^2 s^{-2}	635.72 km^2 s^{-2}
$\langle z^{-2}\rangle$	629.98 km^2 s^{-2}	198.01 km^2 s^{-2}	326.57 km^2 s^{-2}
E_D	−387.01 km^2 s^{-2}	−110.83 km^2 s^{-2}	−208.52 km^2 s^{-2}
L^+	9.17 × 10^8 km^3 s^{-2}	1.13 × 10^8 km^3 s^{-2}	3.31 × 10^8 km^3 s^{-2}
L^-	2.98 × 10^8 km^3 s^{-2}	6.38 × 10^7 km^3 s^{-2}	1.25 × 10^8 km^3 s^{-2}
L_D	−5.08 × 10^8 km^3 s^{-2}	−1.04 × 10^8 km^3 s^{-2}	−1.94 × 10^8 km^3 s^{-2}
T	98071 K	52699 K	60811 K
N	5.69 cm^{-3}	5.66 cm^{-3}	7.43 cm^{-3}
V_{sw}	470.13 km s^{-1}	376.06 km s^{-1}	437.26 km s^{-1}
V_A	91.73 km s^{-1}	47.84 km s^{-1}	69.03 km s^{-1}
$\lvert B\rvert$	8.61 *nT*	4.71 *nT*	7.65 *nT*
ΔUV_A^2	1.93 × 10^6 km^3 s^{-3}	2.29 × 10^5 km^3 s^{-3}	8.25 × 10^5 km^3 s^{-3}

However, a clear decrease in the length of each mfp is found. In the 60:40 case, the averaged $\lambda_\parallel$ is about 0.45 au, and the averaged $\lambda_\perp$ is about 1.07×10^{-3} au. Through analysis of intensity and anisotropy profiles of prompt solar bursts and non-impulsive events, Palmer (1982) finds an mfp consensus: at 1 au, $\lambda_\parallel$ is about 0.08–0.3 au for particles in the rigidity range 0.5–5000 MV. However, the values for mfp's obtained by fitting observational data may depend on the model used (Chhiber et al. 2017). Reames (1999) reviews various events and suggests a higher value of $\lambda_\parallel \sim 1$ au at 1 au. For the $\langle b_{2D}^2\rangle$: $\langle b_s^2\rangle$ = 60: 40 case, $\lambda_\parallel$ in our study is closer to the Palmer consensus range. For the $\langle b_{2D}^2\rangle$: $\langle b_s^2\rangle$ = 80: 20 case, our $\lambda_\parallel$ is closer to Reames' suggested value.

Figure 12 shows the radial evolution of the parallel mfp $\lambda_\parallel$ (blue lines), perpendicular $\lambda_\perp$ (red lines), radial λ_{rr} (cyan lines) mfp, and $\lambda_\perp/\lambda_\parallel$ (green lines) for the years 2003 (solid lines), 2009 (dashed lines), and 2015 (dotted–dashed lines), respectively. Here, we present the radial evolution of the various mfp's for the $\langle b_{2D}^2\rangle$: $\langle b_s^2\rangle$ = 80: 20 outwardly directed IMF mode case only. We solved the coupled 2D and perpendicular slab turbulence transport equations from 1 to 75 au (Adhikari et al. 2017a; Zank et al. 2017; Zhao et al. 2017), using the observed initial conditions for these three years given in Table 2. At 1 au, we use the observed IMF magnitude from Figure 3(e). Beyond 1 au, we employ the Parker spiral magnetic field with a constant SW speed, just as Zhao et al. (2017) assumed. The observed IMF magnitude

Table 2
Initial Conditions at 1 au for the Outwardly Directed IMF

	Year 2003	Year 2009	Year 2015
$\langle z^{+2}\rangle$	593.73 km^2 s^{-2}	221.01 km^2 s^{-2}	379.15 km^2 s^{-2}
$\langle z^{-2}\rangle$	1524.17 km^2 s^{-2}	363.08 km^2 s^{-2}	629.82 km^2 s^{-2}
E_D	-432.79 km^2 s^{-2}	-113.61 km^2 s^{-2}	-201.17 km^2 s^{-2}
L^+	2.41×10^8 km^3 s^{-2}	4.92×10^7 km^3 s^{-2}	1.15×10^8 km^3 s^{-2}
L^-	8.70×10^8 km^3 s^{-2}	1.16×10^8 km^3 s^{-2}	3.25×10^8 km^3 s^{-2}
L_D	-5.38×10^8 km^3 s^{-2}	-8.98×10^7 km^3 s^{-2}	-1.88×10^8 km^3 s^{-2}
T	109,546 K	42,216 K	67,720 K
N	5.33 cm^{-3}	6.02 cm^{-3}	6.96 cm^{-3}
V_{sw}	493.31 km s^{-1}	359.48 km s^{-1}	412.25 km s^{-1}
V_A	88.10 km s^{-1}	43.21 km s^{-1}	66.86 km s^{-1}
$\lvert B\rvert$	8.14 nT	4.41 nT	7.42 nT
ΔUV_A^2	1.93×10^6 km^3 s^{-3}	2.29×10^5 km^3 s^{-3}	8.25×10^5 km^3 s^{-3}

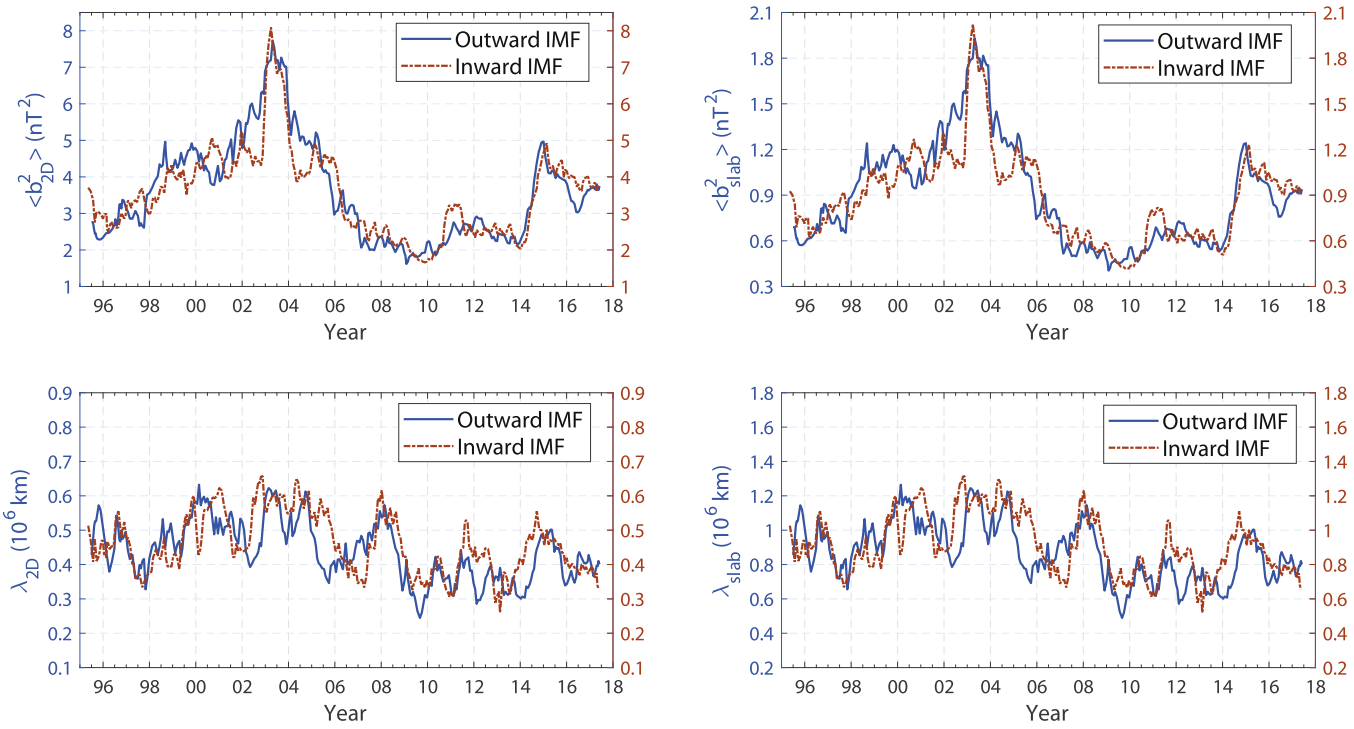

Figure 7. Temporal evolution of the monthly averaged 2D turbulence magnetic energy $\langle b_{2D}^2\rangle$ (top left) and the corresponding correlation length λ_{2D} (bottom left), and the slab turbulence magnetic energy $\langle b_s^2\rangle$ (top right) and the corresponding correlation length λ_s (right bottom). The red dashed lines depict the results calculated for the inwardly directed IMF, and the blue lines for the outwardly directed IMF. A ratio of 2D and slab energy of 80:20 and $\lambda_s = 2\lambda_{2D} = 2\lambda$ have been assumed.

beyond 1 au may be needed in a future study. The radial evolution of the CR diffusion tensor has been described in detail in Zhao et al. (2017). Here, we focus on the effect of solar activity on CR diffusion only. Since the current solar cycle is the weakest of the century, as known so far, the solar activity level for the years 2003 (solar maximum), 2015 (weaker solar maximum), and 2009 (solar minimum) is gradually weakening. Because of this, the parallel mfp $\lambda_\parallel$ increases and the perpendicular mfp $\lambda_\perp$ decreases accordingly for 2003 (solid line), 2015 (dotted–dashed line), and 2009 (dashed line). Beyond ~10 au, such an anti-correlation with solar activity for $\lambda_\parallel$ becomes less clear.

4. Summary and Conclusions

We present a detailed analysis of both large-scale background plasma variables and small-scale Elsässer variables to investigate the effect of solar cycle on SW turbulence parameters and the related CR diffusion coefficients. Compared to previous empirical time-dependent solutions (e.g., Adhikari et al. 2014), we use the *OMNI* 1 minute resolution data over the last two solar cycles to study the temporal evolution of various turbulence quantities at 1 au for the inwardly and outwardly directed IMF, respectively. The SW proton temperature, velocity, Alfvén speed, and IMF magnitude are all positively related to solar activity. There is some anti-correlation between SW temperature and density, but it is not clear in the current solar cycle 24. The fluctuating magnetic energy densities $\langle z^{\pm 2}\rangle$ and the residual energy E_D all exhibit an obvious solar cycle dependence. This is consistent with previous studies (Hnat et al. 2007; Kiyani et al. 2007) that show a solar cycle dependence for magnetic energy density fluctuations within the inertial range, using *Wind* and *ACE* measurements. The value of $\langle z^{+2}\rangle$ for the inwardly directed IMF mode is approximately equal to $\langle z^{-2}\rangle$ for the outwardly directed IMF mode, and vice versa, which can be explained through their definition

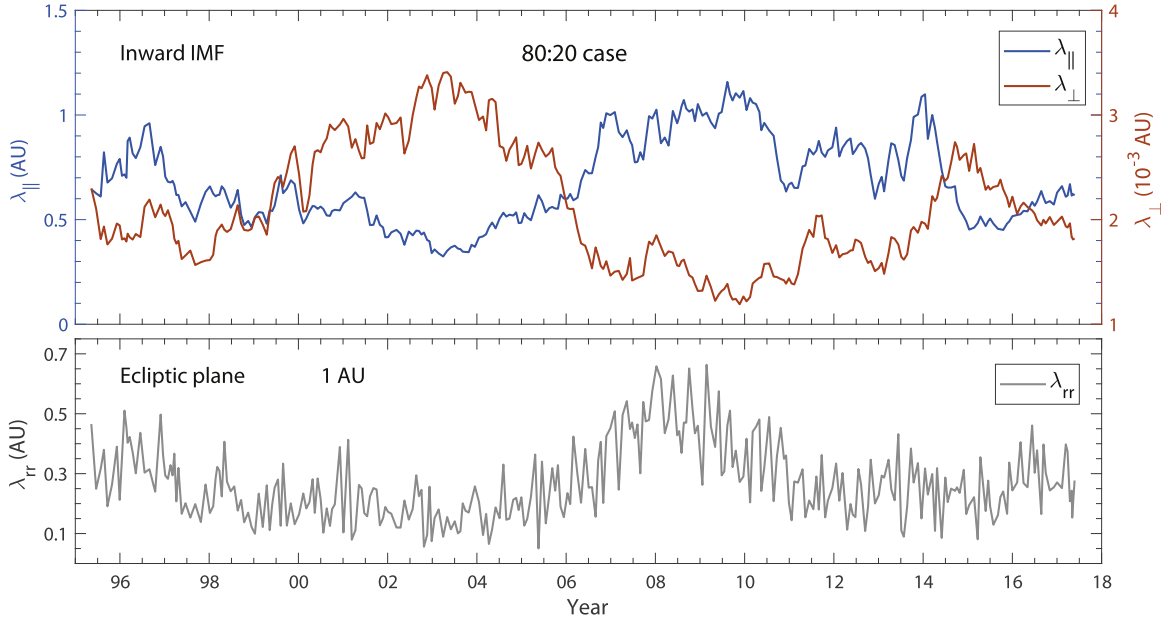

Figure 8. Temporal evolution of CR parallel $\lambda_{||}$ (blue line), perpendicular $\lambda_{\perp}$ (red line), and radial λ_{rr} (gray line) mean free paths for a proton with rigidity 445 MV (corresponding to a 100 MeV proton) in the ecliptic plane at 1 au for inwardly directed IMF. A ratio of 2D and slab energy of 80:20 and $\lambda_s = 2\lambda_{2D} = 2\lambda$ have been assumed. For this example, we have assumed that the background IMF magnitude is constant, $B_0 = 5.5$ nT.

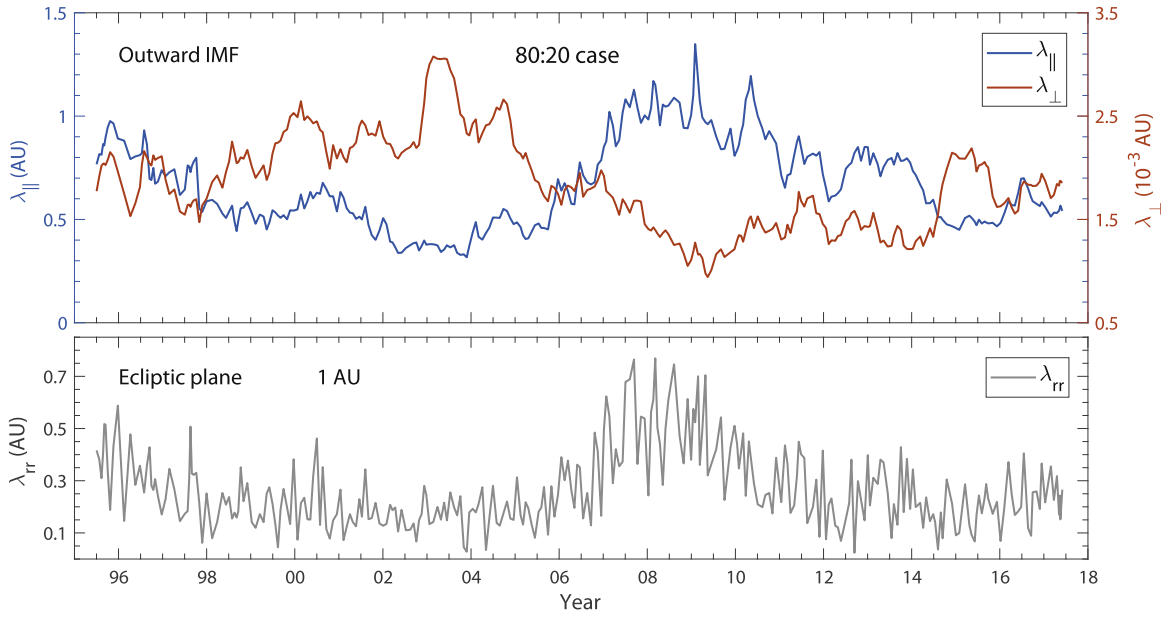

Figure 9. Same as Figure 8, but now for the outwardly directed IMF.

(Equations (4) and (5)). The residual energy E_D, which represents the energy difference between the velocity fluctuations and magnetic field fluctuations (Equation (6)), is always negative for both inwardly and outwardly directed IMF modes. This illustrates that the energy in magnetic fluctuations is larger than the energy in kinetic fluctuations, especially at solar maximum (Figures 4(e) and 5(e)). We introduce the correlation function L^+, L^-, and L_D for the Elsässer variables $z^{\pm}$ and the lagged variables $z^{\pm\prime}$ to calculate the correlation length λ of the magnetic field fluctuations through Equation (11). We find that the correlation functions evolve similarly to the corresponding energy densities $\langle z^{\pm 2}\rangle$ or the residual energy E_D, and are also correlated or anti-correlated with solar cycle. It indicates that the correlation length λ for magnetic fluctuations may not be sensitive to solar cycle. As shown in Figure 7, the correlation length for slab turbulence λ_s (assuming $\lambda_s = 2\lambda_{2D} = 2\lambda$), of which the average value is about 0.88×10^6 km, does not show a significant variation with the solar cycle. One can increase the value of the correlation length by using a longer interval length, but it may introduce some structures associated with large-scale flows (Shiota et al. 2017). The magnetic turbulence energy in 2D $\langle b_{2D}^2\rangle$ and slab $\langle b_s^2\rangle$ fluctuations is positively correlated with the solar cycle. The magnetic turbulence energy $\langle b^2\rangle$ in the year 2003 (solar maximum) is almost four times larger than in 2009 (solar minimum), and also 1.5 times larger than in 2015 (weak solar maximum). There is little difference between the inwardly and outwardly directed IMF modes in the evolution of these turbulence

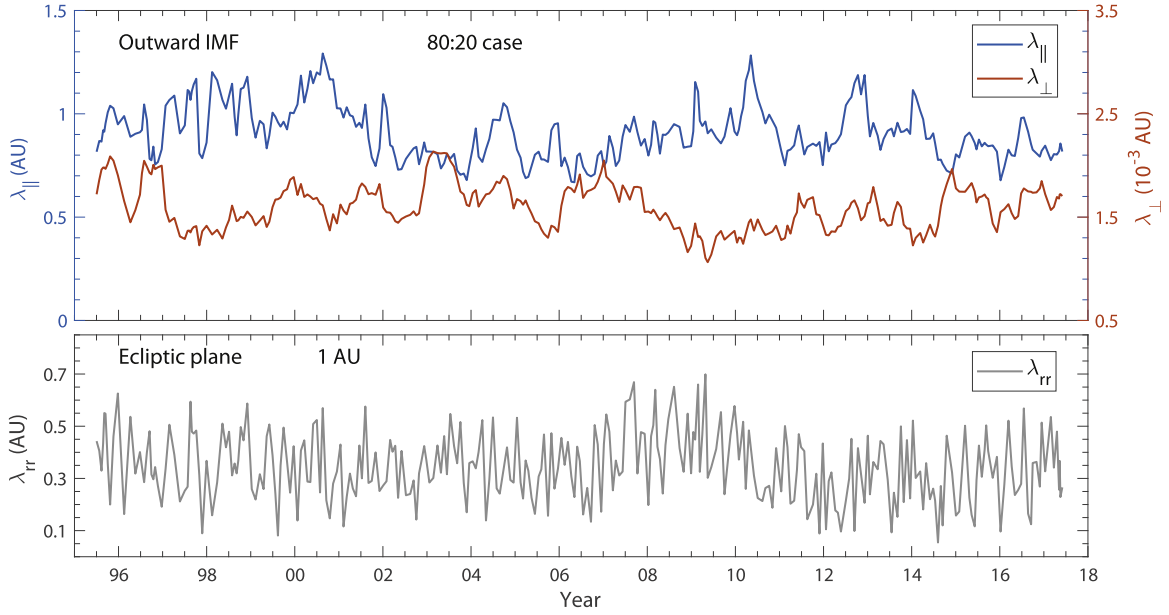

Figure 10. Same as Figure 9, but now for a solar-cycle-dependent background IMF magnitude obtained from Figure 3(e).

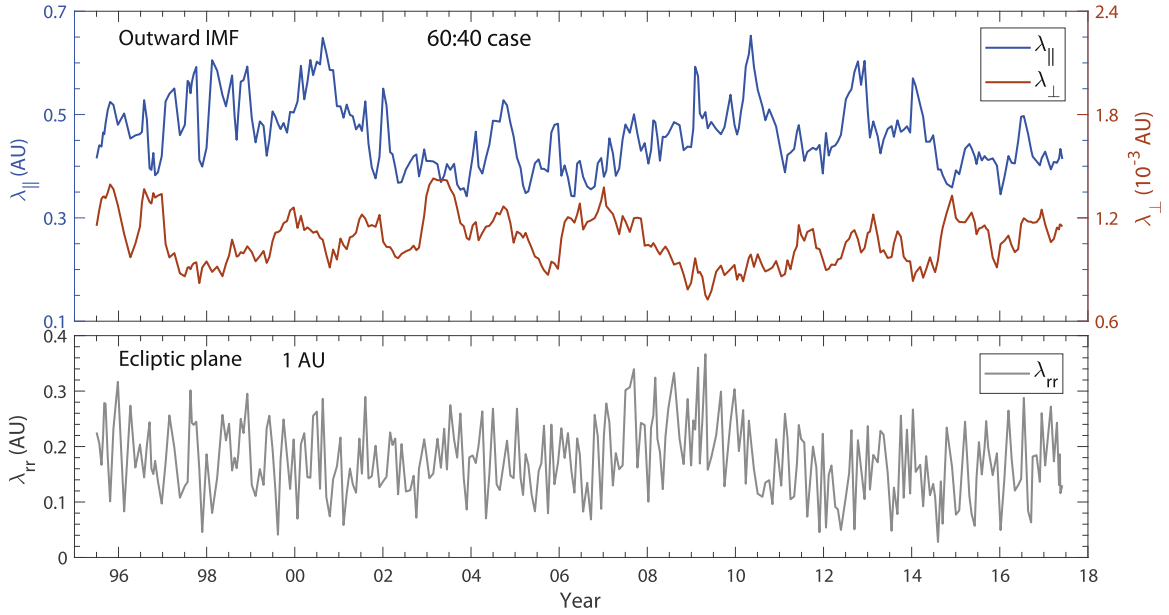

Figure 11. Same as Figure 10, but now for a 60:40 energy ratio between 2D and slab fluctuations.

quantities, which illustrates that the small-scale fluctuations may not depend on the direction of the background magnetic field. Finally, the temporally varying shear source of turbulence, which is most important in the inner heliosphere, also depends on solar cycle.

The above solar-cycle-dependent turbulence quantities at 1 au can be used as input for both turbulence transport models, which in turn describe the radial evolution of such quantities and CR diffusion models. To investigate the solar cycle variation of CR parallel and perpendicular diffusion, one should consider the variation of both turbulence quantities and background large-scale IMF magnitude. We employ QLT and NLGC theory to model the CR parallel mfp $\lambda_{\parallel}$ and the perpendicular mfp $\lambda_{\perp}$, respectively. The temporal evolution of $\lambda_{\parallel}$, $\lambda_{\perp}$, and λ_{rr} in the ecliptic plane at 1 au over the two recent solar cycles is calculated. The parallel mfp $\lambda_{\parallel}$ is about three orders of magnitude larger than the perpendicular mfp $\lambda_{\perp}$, and dominates the radial mfp λ_{rr}. When we use a fixed value of the IMF, the CR mfp's all have a clear solar cycle dependence. The parallel mfp $\lambda_{\parallel}$ and radial mfp λ_{rr} are anti-correlated with the solar cycle while the perpendicular mfp $\lambda_{\perp}$ is positively correlated with the solar cycle. This illustrates that high levels of SW fluctuations will increase CR perpendicular diffusion and decrease parallel diffusion if the background IMF strength remains unchanged. However, if the background IMF changes in concert with the turbulence levels in response to solar activity, this trend can be masked. We also show the effect of using different 2D and slab energy ratios, such as 80%:20% and 60%:40%, which are reasonable according to the observed anisotropy in slow and intermediate SW turbulence. We find that the 60:40 case can yield a much smaller CR parallel mfp, which is closer to the Palmer (1982) consensus. Finally, based

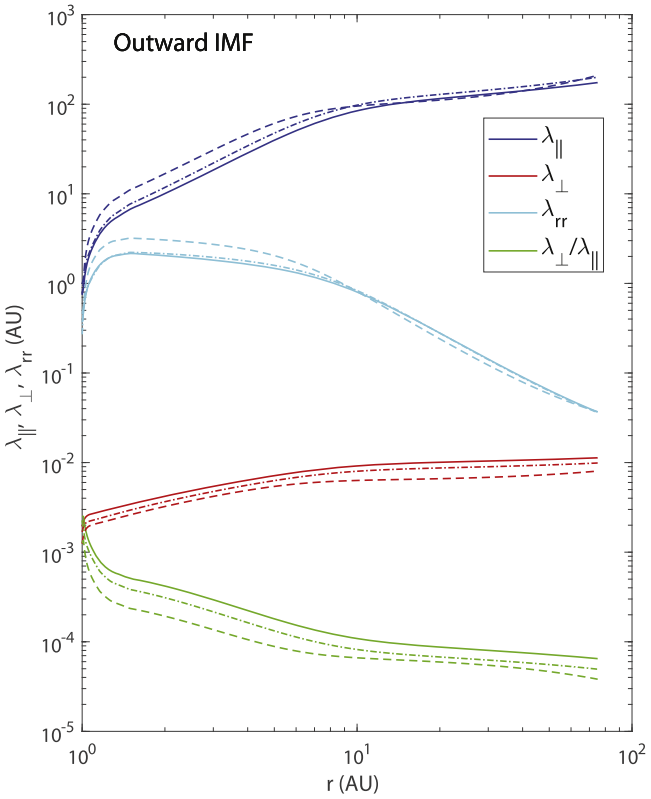

Figure 12. Radial evolution of CR parallel $\lambda_{\parallel}$ (blue lines), perpendicular $\lambda_{\perp}$ (red lines), and radial λ_{rr} (cyan lines) mean free paths for a proton with rigidity of 445 MV for the outwardly directed IMF. The solid lines depict the results for year 2003, the dashed lines the results for year 2009, and the dotted–dashed lines the results for year 2015. A ratio of 2D and slab energy of 80:20 and $\lambda_s = 2\lambda_{2D} = 2\lambda$ have been assumed. The solar-cycle-dependent background IMF magnitude at 1 au is obtained from Figure 3(e).

on the Zank et al. (2017) NI MHD turbulence model, we present the radial evolution of the CR diffusion coefficients from 1 to 75 au. The values of the input parameters needed for the inner boundary conditions for the 2D and slab turbulence models are obtained from observational data at 1 au. The detailed radial properties for the various CR mfp's are given in Zhao et al. (2017). Here, we choose 2003 (strong solar maximum), 2015 (weak solar maximum), and 2009 (solar minimum) to represent three particular epochs of solar activity. With the gradual weakening of the level of solar activity, the value of the parallel mfp $\lambda_{\parallel}$ increases until ~10 au while the perpendicular mfp $\lambda_{\perp}$ decreases throughout the heliosphere. Solar-cycle-dependent boundary conditions lead to solar cycle-related changes in the turbulence quantities and hence in the CR diffusion coefficients. L. Adhikari et al. (2018, in preparation) will present the radial evolution of the turbulence quantities using different boundary conditions related to solar activity at 1 au.

In this study, we present the effect of solar activity cycle on various turbulence quantities and the related CR diffusion coefficients using *OMNI* observations over 22 years. These results provide quantitative input for both CR propagation models and turbulence transport models, and also provide useful insight for time-dependent turbulence modeling to understand the long-term CR modulation which requires turbulence quantities over at least one solar cycle. The solar cycle influence on the global properties of turbulence beyond 1 au still needs further investigation.

This work is partially supported by the National Science Foundation of China under grant No. 41504133, No. 41531073, and No. 41304137. L.L.Z. gratefully acknowledges financial support from the China Scholarship Council, and thanks G.P. Zank for his kind hospitality while visiting the CSPAR-UAH. G.P.Z. and L.A. acknowledge the partial support of NASA grants NNX08AJ33G, Subaward 37102-2, NNX14AC08G, NNX14AJ53G, A99132BT, RR185-447/4944336, and NNX12AB30G. G.P.Z. is partly supported by the International Space Science Institute (ISSI), both through the award of the 2017 Johannes Geiss Fellowship and in the framework of an International Team Project 504 entitled "Current Sheets, Turbulence, Structures and Particle Acceleration in the Heliosphere." Q.H. acknowledge partial support from SAO subcontract SV4-84017 and NASA grant NNX17AB85G. This work is supported in part by the NSF EPSCOR RII-Track-1 Cooperative Agreement OIA-1655280.

ORCID iDs

L.-L. Zhao https://orcid.org/0000-0002-4299-0490
L. Adhikari https://orcid.org/0000-0003-1549-5256
G. P. Zank https://orcid.org/0000-0002-4642-6192
Q. Hu https://orcid.org/0000-0002-7570-2301
X. S. Feng https://orcid.org/0000-0001-8605-2159

References

Adhikari, L., Zank, G. P., Bruno, R., et al. 2015, ApJ, 805, 63
Adhikari, L., Zank, G. P., Hu, Q., & Dosch, A. 2014, ApJ, 793, 52
Adhikari, L., Zank, G. P., Hunana, P., et al. 2017a, ApJ, 841, 85
Adhikari, L., Zank, G. P., Hunana, P., & Hu, Q. 2016, ApJ, 833, 218
Adhikari, L., Zank, G. P., Telloni, D., et al. 2017b, ApJ, 851, 117
Adriani, O., Barbarino, G. C., Bazilevskaya, G. A., et al. 2016, PhRvL, 116, 241105
Bame, S. J., Asbridge, J. R., Feldman, W. C., & Gosling, J. T. 1976, ApJ, 207, 977
Bieber, J. W., Burger, R. A., & Matthaeus, W. H. 1995, Proc. ICRC, 4, 694
Bieber, J. W., Chen, J., Matthaeus, W. H., et al. 1991, JGR, 98, 3585
Bieber, J. W., Matthaeus, W. H., Shalchi, A., & Qin, G. 2004, GeoRL, 31, L10805
Bieber, J. W., Wanner, W., & Matthaeus, W. H. 1996, JGR, 101, 2511
Breech, B., Matthaeus, W. H., Minnie, J., et al. 2008, JGR, 113, A08105
Burger, R. A., Krüger, T. P. J., Hitge, M., & Engelbrecht, N. E. 2008, ApJ, 674, 511
Burger, R. A., Nel, A. E., & Engelbrecht, N. E. 2014, in AGU Fall Meeting Abstracts (San Francisco, CA: AGU), SH51A-4152
Burger, R. A., Potgieter, M. S., & Heber, B. 2000, JGR, 105, 27447
Burlaga, L. F., Ness, N. F., Wang, Y.-M., & Sheeley, N. R. 2002, JGR, 107, 1410
Chen, C. H. K., Mallet, A., Yousef, T. A., Schekochihin, A. A., & Horbury, T. S. 2011, MNRAS, 415, 3219
Chhiber, R., Subedi, P., Usmanov, A. V., et al. 2017, ApJ, 230, 21
Cho, J., & Vishniac, E. T. 2000, ApJ, 539, 273
Dasso, S., Milano, L. J., Matthaeus, W. H., & Smith, C. W. 2005, ApJL, 635, L181
Dosch, A., Adhikari, L., & Zank, G. P. 2013, in AIP Conf. Proc. 1539, Solar Wind 13, ed. G. P. Zank et al. (Melville, NY: AIP), 155
Du, Z. 2012, SoPh, 278, 203
Duffy, P., & Blundell, K. M. 2005, PPCF, 47, B667
Effenberger, F., Fichtner, H., Scherer, K., et al. 2012, ApJ, 750, 108
Elsässer, W. M. 1950, PhRv, 79, 183
Engelbrecht, N. E. 2017, ApJL, 849, L15
Engelbrecht, N. E., & Burger, R. A. 2013a, ApJ, 772, 46
Engelbrecht, N. E., & Burger, R. A. 2013b, ApJ, 779, 158
Engelbrecht, N. E., & Burger, R. A. 2015, ApJ, 814, 152
Ferreira, S. E. S., & Potgieter, M. S. 2004, ApJ, 603, 744
Florinski, V., Zank, G. P., & Pogorelov, N. V. 2003, JGR, 108, 1228
Gazis, P. R., Barnes, A., & Mihalov, J. D. 1995, SSRv, 72, 117
Giacalone, J., & Jokipii, J. R. 1999, ApJ, 520, 204
Goldstein, M. L., & Roberts, D. A. 1999, PhPl, 6, 4154

Guo, X., & Florinski, V. 2016, ApJ, 826, 65
Hnat, B., Chapman, S. C., Kiyani, K., Rowlands, G., & Watkins, N. W. 2007, GeoRL, 34, L15108
Hunana, P., & Zank, G. P. 2010, ApJ, 718, 148
Hunana, P., Zank, G. P., Heerikhuisen, J., & Shaikh, D. 2008, JGR, 113, A11105
Isenberg, P. A. 2005, ApJ, 623, 502
Isenberg, P. A., Smith, C. W., Matthaeus, W. H., & Richardson, J. D. 2010, ApJ, 719, 716
Jian, L., Russell, C. T., Luhmann, J. G., & Skoug, R. M. 2006, SoPh, 239, 337
Jian, L. K., Russell, C. T., & Luhmann, J. G. 2011, SoPh, 274, 321
Jokipii, J. R. 1966, ApJ, 146, 480
Jokipii, J. R., & Kóta, J. 2000, Ap&SS, 274, 77
Kiyani, K., Chapman, S. C., Hnat, B., & Nicol, R. M. 2007, PhRvL, 98, 211101
Kolmogorov, A. 1941, DoSSR, 30, 301
Kryukov, I. A., Pogorelov, N. V., Zank, G. P., & Borovikov, S. N. 2012, in AIP Conf. Proc. 1436, Physics of the Heliosphere, ed. J. Heerikhuisen (Melville, NY: AIP), 48
Le Roux, J. A., & Potgieter, M. S. 1995, ApJ, 442, 847
Manuel, R., Ferreira, S. E. S., Potgieter, M. S., Strauss, R. D., & Engelbrecht, N. E. 2011, AdSpR, 47, 1529
Marino, R., Sorriso-Valvo, L., Carbone, V., et al. 2008, ApJL, 677, L71
Matthaeus, W. H., Bieber, J. W., Ruffolo, D., Chuychai, P., & Minnie, J. 2007, ApJ, 667, 956
Matthaeus, W. H., Dasso, S., Weygand, J. M., et al. 2005, PhRvL, 95, 231101
Matthaeus, W. H., Qin, G., Bieber, J. W., et al. 2003, ApJL, 590, L53
Matthaeus, W. H., Servidio, S., Dmitruk, P., et al. 2012, ApJ, 750, 103
Matthaeus, W. H., Weygand, J. M., Chuychai, P., et al. 2008, ApJL, 678, L141
Matthaeus, W. H., Zank, G. P., & Oughton, S. 1996, JPlPh, 57, 659
Matthaeus, W. H., Zank, G. P., Smith, C. W., & Oughton, S. 1999, PhRvL, 82, 3444
Matthaeus, W. H., Zhou, Y., Zank, G. P., & Oughton, S. 1994, JGR, 99, 23
Milano, L. J., Matthaeus, W. H., Dmitruk, P., & Montgomery, D. C. 2001, PhPl, 8, 2673
Minnie, J., Bieber, J. W., Matthaeus, W. H., & Burger, R. A. 2007, ApJ, 670, 1149
Morfill, G. E., & Völk, H. J. 1979, JGR, 84, 4446
Osman, K. T., & Horbury, T. S. 2007, ApJL, 654, L103
Oughton, S., Dmitruk, P., & Matthaeus, W. H. 2006, PhPl, 13, 042306
Oughton, S., Matthaeus, W. H., Smith, C. W., Breech, B., & Isenberg, P. A. 2011, JGR, 116, 8105
Oughton, S., Matthaeus, W. H., Wan, M., & Osman, K. T. 2015, RSPTA, 373, 20410152
Palmer, I. D. 1982, RvGeo, 20, 335
Parker, E. N. 1958, ApJ, 128, 664
Parker, E. N. 1965, P&SS, 13, 9
Pei, C., Bieber, J. W., Breech, B., et al. 2010, JGR, 115, A03103
Potgieter, M. S. 1998, SSRv, 83, 147
Potgieter, M. S. 2013, LRSP, 10, 3
Potgieter, M. S., & Vos, E. E. 2016, Journal of Physics: Conference Series, 767, 012018
Potgieter, M. S., Vos, E. E., Munini, R., Boezio, M., & Di Felice, V. 2015, ApJ, 810, 141
Reames, D. V. 1999, SSRv, 90, 413
Richardson, J. D., & Smith, C. W. 2003, GeoRL, 30, 1206
Ruffolo, D., Painpanit, T., Matthaeus, W. H., & Chuychai, P. 2012, ApJL, 747, L34
Ruiz, M. E., Dasso, S., Matthaeus, W. H., Marsch, E., & Weygand, J. M. 2011, JGRA, 116, A10102
Shalchi, A. 2005, PhPl, 12, 052324
Shalchi, A. 2009, Nonlinear Cosmic Ray Diffusion Theories, Vol. 362 (Berlin: Springer)
Shalchi, A. 2013, ApJ, 774, 7
Shalchi, A., Bieber, J. W., & Matthaeus, W. H. 2004, ApJ, 604, 675
Shalchi, A., & Kourakis, I. 2007, PhPl, 14, 112901
Shalchi, A., Li, G., & Zank, G. P. 2010, Ap&SS, 325, 99
Shiota, D., Zank, G. P., Adhikari, L., et al. 2017, ApJ, 837, 75
Smith, C. W. 2003, in AIP Conf. Proc. 679, Solar Wind 10, ed. M. Velli et al. (Melville, NY: AIP), 413
Smith, C. W., Isenberg, P. A., Matthaeus, W. H., & Richardson, J. D. 2006, ApJ, 638, 508
Smith, C. W., Matthaeus, W. H., Zank, G. P., et al. 2001, JGR, 106, 8253
Sonnerup, B. U. Ö, & Scheible, M. 1998, ISSIR, 1, 185
Strauss, R. D., Potgieter, M. S., & Ferreira, S. E. S. 2012, AdSpR, 49, 392
Teufel, A., & Schlickeiser, R. 2002, A&A, 393, 703
Tu, C.-Y., & Marsch, E. 1995, SSRv, 73, 1
Usmanov, A. V., Goldstein, M. L., & Matthaeus, W. H. 2014, ApJ, 788, 43
Usmanov, A. V., Matthaeus, W. H., Breech, B. A., & Goldstein, M. L. 2011, ApJ, 727, 84
Verma, M. K., Roberts, D. A., & Goldstein, M. L. 1995, JGR, 100, 19839
Völk, H. J., Morfill, G., Alpers, W., & Lee, M. A. 1974, Ap&SS, 26, 403
Weygand, J. M., Matthaeus, W. H., Dasso, S., et al. 2009, JGR, 114, A07213
Weygand, J. M., Matthaeus, W. H., Dasso, S., & Kivelson, M. G. 2011, JGRA, 116, A08102
Wheatland, M. S., & Litvinenko, Y. E. 2001, ApJ, 557, 332
Wicks, R. T., Chapman, S. C., & Dendy, R. O. 2009, ApJ, 690, 734
Wiengarten, T., Oughton, S., Engelbrecht, N. E., et al. 2016, ApJ, 833, 17
Williams, L. L., Zank, G. P., & Matthaeus, W. H. 1995, JGR, 100, 17059
Zank, G. P., Adhikari, L., Hunana, P., et al. 2017, ApJ, 835, 147
Zank, G. P., Adhikari, L., Hunana, P., et al. 2018, ApJ, 854, 32
Zank, G. P., Dosch, A., Hunana, P., et al. 2012, ApJ, 745, 35
Zank, G. P., Li, G., Florinski, V., et al. 2004, JGR, 109, A04107
Zank, G. P., & Matthaeus, W. H. 1991, PhFlA, 3, 69
Zank, G. P., & Matthaeus, W. H. 1992, JGR, 97, 17189
Zank, G. P., & Matthaeus, W. H. 1993, PhFl, A5, 257
Zank, G. P., Matthaeus, W. H., & Bieber, J. W. 1998, JGR, 103, 2085
Zank, G. P., Matthaeus, W. H., & Smith, C. W. 1996, JGR, 101, 17093
Zhang, M. 1999, ApJ, 513, 409
Zhao, L. L., Adhikari, L., Zank, G. P., Hu, Q., & Feng, X. S. 2017, ApJ, 849, 88
Zhao, L. L., & Qin, G. 2013, JGR, 118, 1837
Zhao, L. L., Qin, G., Zhang, M., & Heber, B. 2014, JGR, 119, 1493
Zhao, L. L., & Zhang, H. 2015, ApJ, 805, 6
Zhao, L. L., & Zhang, H. 2016, ApJ, 827, 13
Zheng, J., & Hu, Q. 2018, ApJL, 852, L23
Zhou, Y., & Matthaeus, W. H. 1990a, JGR, 95, 14881
Zhou, Y., & Matthaeus, W. H. 1990b, JGR, 95, 14863